ResearchGate

See discussions, stats, and author profiles for this publication at: https://www.researchgate.net/publication/251734853

The energy balance at substrate surfaces during plasma processing

Article *in* Vacuum · August 2001

Impact Factor: 1.86 · DOI: 10.1016/S0042-207X(01)00350-5

CITATIONS
171

READS
128

5 authors, including:

Holger Kersten
Christian-Albrechts-Universität zu Kiel
218 PUBLICATIONS **1,831** CITATIONS

SEE PROFILE

G.M.W. Kroesen
Technische Universiteit Eindhoven
258 PUBLICATIONS **3,867** CITATIONS

SEE PROFILE

Rainer Hippler
University of Greifswald
340 PUBLICATIONS **3,623** CITATIONS

SEE PROFILE

All in-text references underlined in blue are linked to publications on ResearchGate, letting you access and read them immediately.

Available from: Rainer Hippler
Retrieved on: 12 May 2016

PERGAMON

Vacuum 63 (2001) 385–431

VACUUM
SURFACE ENGINEERING, SURFACE INSTRUMENTATION & VACUUM TECHNOLOGY

www.elsevier.com/locate/vacuum

The energy balance at substrate surfaces during plasma processing

H. Kersten[a,*], H. Deutsch[a], H. Steffen[a], G.M.W. Kroesen[b], R. Hippler[a]

[a] *Institute for Physics, E.-M.-Arndt-University, Domstrasse 10a, 17487 Greifswald, Germany*
[b] *Department of Physics, TU Eindhoven, P.O. Box 513, 5600 MB Eindhoven, Netherlands*

Abstract

A summary is given of different elementary processes influencing the thermal balance and energetic conditions of substrate surfaces during plasma processing. The discussed mechanisms include heat radiation, kinetic and potential energy of charged particles and neutrals as well as enthalpy of involved chemical surface reactions. The energy and momentum of particles originating from the plasma or electrodes, respectively, influence via energy flux density (energetic aspect) and substrate temperature (thermal aspect) the surface properties of the treated substrates. The various contributions to the energy balance are given in a modular mathematical framework form and examples for an estimation of heat fluxes and numerical values of relevant coefficients for energy transfer, etc. are given.

For a few examples as titanium film deposition by hollow cathode arc evaporation, silicon etching in CF_4 glow discharge, plasma cleaning of contaminated metal surfaces, and magnetron sputtering of aluminum the energetic balance of substrates during plasma processing will be presented. Furthermore, the influence of the resulting substrate temperature on characteristic quantities as etching or deposition rates, layer density, microstructure, etc. will be illustrated for some examples, too. © 2001 Elsevier Science Ltd. All rights reserved.

1. Introduction

At present plasma processing of materials is one of the fastest growing branches in plasma physics and has got a prominent position in the rather new field of applied surface science. In particular, plasma–wall interactions are of great importance in a large variety of applications of low-temperature, low-pressure plasmas in such fields as etching, deposition and surface modification of thin films. In these processes the thermal and energetic conditions at the substrate surface play a dominant role.

In detail, low-temperature plasma processing of solid surfaces is mainly affected by the following parameters:

- energy per incoming particle (E_v), which is related to energy transfer,
- particle flux density to the substrate (j_v), which is related to momentum transfer,
- energy flux density ($J_v = j_v E_v$), representing a key parameter for the energetic conditions at the surface, and
- temperature of the substrate surface (T_S), which results from the inner parameters (E_v, J_v) mentioned above and which reflects the thermal

*Corresponding author. Tel.: +49-3834-864-752; fax: +49-3834-864-701.
E-mail address: kersten@physik.uni-greifswald.de (H. Kersten).

0042-207X/01/$ - see front matter © 2001 Elsevier Science Ltd. All rights reserved.
PII: S0042-207X(01)00350-5

balance at the surface as a macroscopic quantity.

The surface temperature T_S, which can also be influenced by external heating, effects elementary processes like adsorption, desorption and diffusion as well as chemical reactions (chemical sputtering, surface film reaction) [1–4].

On the other hand, especially in the case of thin film deposition, the structure and morphology as well as the stoichiometry of the film depend strongly on the energetic conditions (J_v) at the surface, see for example [1,5–10]. The surface diffusion of adsorbed atoms can be enhanced, which may result in a rearrangement of deposited atoms [11,12]. Bombardment of a growing film with low-energy ions results in a modification of its properties, see for example [13].

It should be emphasized, that in addition to external heating the surface temperature T_S is influenced by the energy flux resulting from energetic particle bombardment, chemical surface reactions and heat radiation [14–17]. By a suitable variation of the experimental conditions the different contributions to substrate heating can be separated and studied independently.

In general, the energy transfer between plasma and solid is a very complex mechanism. In the case of thermal plasmas the transfer can be described by means of classical terms as thermal conductivity and heat transfer coefficients. However, for non-equilibrium plasmas such an approach is not possible because the term "heat" has no precise meaning. In those plasmas the thermal conditions at the surface must be described by a detailed energy balance, which considers the different heat sources and heat losses [18–21].

Besides radiation from the environment (plasma, walls), the energy fluxes consist of kinetic energy and potential energy of the incoming particles. The distribution of the several energetic contributions depends on the discharge conditions and the substrate potential. Therefore, the experimental investigation of plasma–wall interaction due to energy transfer in technological plasma processing requires sophisticated measurements [20,21].

In the first part of the present paper we will attempt to give a methodological description of relevant channels for substrate heating and surface modification, respectively, and their transfer mechanisms. Such a general description shall help to estimate the energy transfer from plasmas to solid surfaces and, thus, the estimation of the thermal conditions at substrates during plasma processing. In the following section (Section 3) various methods for an experimental determination of thermal quantities as heat fluxes and surface temperature are described.

In order to illustrate the influence of the thermal and energetic conditions at the substrate surface, in Section 4 some examples for temperature dependencies of etching and deposition as well as for the changes of the surface properties by energetic particle bombardment are presented. Finally, implementations of the models for a few specific, experimentally studied plasma–substrate systems will be described in this part. Examples for such systems are plasma polymerization of benzene, deposition of TiN_x by hollow cathode arc evaporation, magnetron sputtering of thin aluminum films, CF_4-plasma etching of silicon, and plasma cleaning of lubricant-contaminated metal surfaces.

2. Energy balance at the substrate surface

2.1. Contributions to the integral energy influx

When a plasma acts on a solid surface the surfaces are heated due to energy transfer which can be described by a balance of the involved energy fluxes. In general, the total power input $\dot{Q}_{in}$ at the substrate surface is the surface integral over the sum of different contributions J_v (energy flux per time and area):

$$\dot{Q}_{in} = \int (J_{rad,1} + J_{ch} + J_n + J_{ads} + J_{react,1} + J_{ext,1})\,\mathrm{d}A. \tag{1}$$

$J_{rad,1}$ is the heat radiation towards the surface, J_{ch} is the power transfered by charge carriers (electrons and ions), and J_n is the contribution of neutral species of the background gas and the neutral particles contributing to the film growth. The latter terms in Eq. (1) are energy released by

adsorption or condensation (J_{ads}) and the reaction energy of exothermic processes including molecular surface recombination ($J_{react,1}$). Additionally, also power input by external sources ($J_{ext,1}$) influences the thermal balance of the substrate.

In the following the different contributions to the integral heat influx during low-temperature plasma processing will be described in a general way.

2.1.1. Heat radiation ($J_{rad,1}$)

Radiative energy sources in plasma processing might be the surrounding surfaces (e.g. reactor walls, enclosure), hot material sources (e.g. crucibles) and the gas/plasma radiation itself. Hence, heat radiation $J_{rad,1}$ becomes important in high-temperature plasmas and/or if the temperature of the reactor walls is high due to external heating as for example in plasma enhanced chemical vapor deposition (PECVD). Also in evaporation processes where molten materials are employed for thin film deposition (e.g. electron beam evaporation, hollow cathode arc evaporation [20]) the heat radiation of the crucible can be an essential contribution to the global energy balance of the substrate treated.

The heat radiation $J_{rad,1}$ from such a hot source can be generally written as

$$J_{rad,1} = \int \varepsilon(\lambda, T_{rad})\alpha_S(\lambda, T_S)W(\lambda, T_{rad})A_{rad} f(A_{rad}, A_S)\,\mathrm{d}\lambda \approx \sigma(\varepsilon T_{rad}^4 - \varepsilon_S T_S^4) \tag{2}$$

Here $\varepsilon(\lambda, T_{rad})$ is the spectral emittance of the radiation source at temperature T_{rad} and $\alpha_S(\lambda, T_S)$ represents the spectral absorptance of the substrate surface at temperature T_S. $W(\lambda, T_{rad})$ is the Planck radiant emittance at T_{rad}, while $\sigma = 5.67\times10^{-8}\,\mathrm{W\,m^{-2}\,K^{-4}}$ denotes the Stefan–Boltzmann constant and λ the wavelength. The factor $f(A_{rad}, A_S)$ marks a configuration factor for radiation traveling from the radiation source (e.g. crucible) of an area A_{rad} to the substrate of an area A_S, which can be assumed in the most simple case as $f(A_{rad}, A_S) \sim 1/d^2$ (d the distance between heat source and substrate).

In general, Eq. (2) involves terms containing complicate integrals concerning the wavelength and the configuration factor. In order to simplify the integral two assumptions should be made [15]:

1. the emissivity of radiation sources (reactor wall, materials in the crucible) is independent of the wavelength λ and the grey-body assumption is used in the derivation of Stefans's law,
2. the spectral absorptance of the substrate is essentially independent of its temperature.

More detailed analytical methods are employed in global modelling of radiative heat transfer in crystal growth furnaces, see for instance [22]. In view of the geometrical complexity of common plasma reactor systems and the non-linearity of the problem of radiative energy transfer an approach can be based on the net-radiation method. In this method the enclosure of the substrate is divided into a number of isothermal patches, while the radiative transfer is calculated between every pair of such patches. The exchange areas produce the relationships between net fluxes and radiative emitted fluxes, which result in a matrix relationship between net fluxes and fourth powers of temperatures on the enclosure. The cross-section of the radiating areas are mostly simplified by finite symmetric elements.

In a more empirical way, Dey et al. [23] investigated the heat exchange between evaporation source, substrate and enclosure at electron-beam evaporation of silicon films using an electrical model for the first time. This model of radiative heat transfer processes involves resistances representing the bodies of the heat interaction as an electrical circuit.

In most cases it is sufficient to take into account the simplification as, mentioned above, which yields the Boltzmann formula for heat transfer by radiation:

$$J_{rad,1} = \sigma(\varepsilon T_{rad}^4 - \varepsilon_S T_S^4). \tag{3}$$

Usually, the contribution of heat radiation from hot surfaces in a common low-temperature plasma reactor is small, but in some applications in combination with CVD or arc evaporation (like in hollow cathode arc evaporation, see Section 4.1.2) it can amount up to several tens of percent.

Besides radiation from the enclosure walls or evaporation sources there are also radiative contributions from excited species of the plasma in form of photons ranging from IR to UV. However, it is very difficult to measure and to calibrate this contribution on the integral energy flux.

Integration of spectral radiative transfer properties over the entire optical spectrum of complex multi-component plasmas in any point of space taking into consideration variable fields of temperature is practically impossible. In [24] an asymptotic integral method of the so-called "partial characteristics" has been proposed. For a certain plasma with a number of model temperature profiles they calculated spectrum-integral partial characteristics. The characteristics contain a source function and the optical density of the absorption path. This method makes it possible to calculate the divergence of the radiation flux in the volume of any configuration.

In order to study the heat transfer in CVD and PECVD experiments Leroy et al. used coherent anti-Raman–Stokes (CARS) measurements [25]. A one-dimensional thermal model has been developed by the authors to interpret their measured profiles and to determine the temperature of the surfaces which are unknown.

Another general procedure for the evaluation of substrate heating due to resonance radiation is to determine the absorption coefficient for each resonant state and to determine the corresponding escape factor and the effective photon lifetime for each [26]. From the measured electron energy distribution function (EEDF) the rate coefficients for excitation and quenching of these states have to be determined. Finally, based on a particle balance equation for the considered excited state densities, the population of the excited states is calculated and the radiation from the plasma to the substrate surface is obtained. By this method, Piejak et al. [26] estimated the relevant photon fluxes j_{ph} for the resonant states and the radiant power density J_{rad} is

$$J_{rad} = \xi_{ph} j_{ph} E_{ph}. \tag{4}$$

ξ_{ph} is the probability that a photon is absorbed by the surface (taken to be one) and E_{ph} is the average photon energy (11.8 eV for Ar). Eq. (4) provides an upper limit appropriate for a substrate immersed into the plasma glow and positioned away from a plasma sheath. However, even for this rather unrealistic assumption the contribution of the plasma radiation compared to the other thermal influxes at an inductively coupled RF discharge in argon as investigated in [26] was only in the order of 5–10%.

In contrast, in the case of cylindrical magnetron sputtering at rather high energy, the contribution of plasma radiation was estimated by Thornton [16] to be in the order of about 20–30% of the total heat flux depending on the target material.

2.1.2. Energy influx by charge carriers (J_{ch})

For many applications, non-isothermal low-pressure discharges play an important role in plasma processing. In those discharges, the most efficient channel of energy transfer is due to charge carriers, which get their directed kinetic energy by acceleration in the sheath in front of a surface. The width of the sheath is essentially influenced by the discharge type. Depending on gas pressure and discharge power one distinguishes between the so-called α- and γ-regime [27].

Generally, the total energy flux of charged particles J_{ch} is given by the product of the particle flux density (j_e for electrons, j_i for ions) to the substrate surface and the mean particle energy (E_e for electrons, E_i for ions). The energy of the positive and negative ions consists, in general, of a potential and a kinetic part.

In detail, the following components may contribute to the energy influx J_{ch} by charge carriers from the plasma and from the electrodes, respectively, to the substrate during low-temperature, low-pressure plasma processing:

- positive ions (mainly from the plasma of the carrier gas, but also from species of deposition material, products, etc.): $J_{i+} = j_{i+} E_{i+}$,
- negative ions (in case of electronegative process plasmas): $J_{i-} = j_{i-} E_{i-}$,
- recombination of positive ions and electrons at the substrate surface: $J_{rec} = j_{i+} E_{rec}$.
- plasma electrons (or low-energy secondary electrons): $J_e^{slow} = j_e^{slow} E_e^{slow}$,

- beam electrons from the cathode (or high-energy primary electrons): $J_e^{fast} = j_e^{fast} E_e^{fast}$,

$$J_{ch} = J_{i+} + J_{i-} + J_{rec} + J_e^{slow} + J_e^{fast}. \quad (5)$$

The different contributions have been discussed, for example, for magnetron sputtering in [28,29]. Fig. 1 illustrates the potential distribution between cathode, plasma and substrate as well as the resulting fluxes of positive and negative particles in a typical discharge device.

In the following, the contributions of ions and electrons to the integral energy influx will be discussed separately in more detail.

Energy influx by ions (J_{i+}, J_{i-}, J_{rec}). The energy of ions striking the substrate is the sum of potential ($E_{i,pot}$) and kinetic energy $E_{i,kin}$.

Concerning the potential energy of an ion released in plasma wall interaction one must distinguish between conducting or insulating substrates. At first we will discuss the case of a metallic substrate: The neutralization of ions on such surfaces is caused by long-range interactions and is accompanied by the emission of secondary electrons. Then $E_{i,pot}$ is given as

$$E_{i,pot} = E_{ion} - \Phi - \gamma_i(\Phi + E_{i,kin}). \quad (6)$$

($E_{ion} = E_{rec}$ the ionization potential of the incident ion, Φ the work function, γ_i the yield of secondary electrons, $E_{i,kin}$ the mean kinetic energy of incident ion.) Data for E_{ion}, Φ and γ_i, respectively, may be taken from the literature [30,31]. For semiconductors the yield of secondary electron emission is one order of magnitude smaller than for metals [30]. The work function Φ for metals and semiconductors is in the order of $\sim 5\,\text{eV}$ (see for example [31]).

In systems where the heat flux to the surface is dominated by ion bombardment (e.g. in planar RF reactors) the contribution of the potential energy term (Eq. (6)) can be very substantial (several tens of percent) for low kinetic energies [32].

Otherwise, for insulating materials the energy gain per ion is determined by

$$E_{i,pot} = E_{rec} + E_{i,ads}, \quad (7)$$

where $E_{rec} = E_{ion}$ is the recombination energy and $E_{i,ads}$ the adsorption energy of the ions. The neutralization of ions on insulating surfaces proceeds via recombination of the adsorbed positive ions with electrons [33]. In special cases, as for instance the glass walls surrounding a positive column of an inert gas glow discharge [34] and powder particles suspended in an RF plasma [35], the energy gain by recombination may become dominant in surface heating.

In addition to potential energy, ions transfer a part of their kinetic energy when striking a surface. The mean kinetic ion energy $E_{i,kin}$ is determined by the ion energy distribution function (IEDF). The energy distribution of the ions arriving at the substrate is affected by the pressure which influences the collisions in the sheath in front of the substrate, and by the instantaneous, local

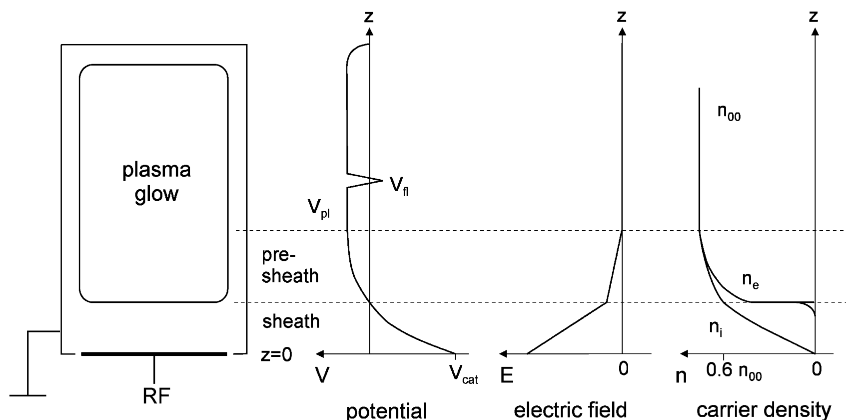

Fig. 1. Potential and field distribution as well as carrier densities which result in fluxes of charge carriers between cathode, plasma, and substrate. (V_{pl} the plasma potential, V_{cat} the potential of the cathode, $V_{fl} = V_S$ the substrate potential.)

electric field. These effects may lead to a broadening, to a shift, and to various shapes of the IEDF. The maximum ion energy is determined by the free fall energy $e_0 V_{sh}$, where V_{sh} is the potential drop across the sheath in front of substrate which corresponds to the sum of the plasma potential V_{pl} and the substrate potential V_S, see also Fig. 1:

$$V_{sh} = V_{bias} = V_{pl} + V_S. \quad (8)$$

The value of the sheath potential is essentially determined by the internal plasma parameter as electron density and the energy distribution of electrons and ions in the plasma. The shape of the IEDF at the substrate is largely influenced by [36,37]:

- collisional processes in the sheath, or more precisely, by the ratio of the mean free path of the ions and the sheath thickness, and
- the frequency of the alternating electric field which determines the ratio of drift time of the ions through the sheath and the half period of the electric field in the case of RF and microwave discharges.

While the collisional processes in the sheath result in a simple broadening at the low-energy part of the energy distribution and in a decrease of the mean energy, the influence of an alternating RF field may result in a complex, saddle-like structure of the IEDF. Fig. 2 represents examples for typical ion energy distribution functions in plasma processing in order to illustrate both effects. Measurements of the ion energy distribution are mainly carried out by energy resolved mass spectrometry (plasma monitoring) where the ions are extracted from the substrate region [21,38]. There exist also a number of theoretical approaches in order to calculate IEDFs based on particle-in-cell simulation [39], Monte Carlo simulation [40], and the development of analytical expressions [38,41].

In addition to the directed kinetic energy of the ions which originates for positive ions from acceleration in the electrical field in front of the substrate, they receive thermal energy $\frac{3}{2}kT_i$, too (k the Boltzmann constant, T_i the ion temperature). As mentioned above, the directed kinetic energy can be assumed in most cases to be approximately equal to the sheath potential $e_0 V_{sh} = e_0 V_{bias}$. Hence, the total kinetic energy of positive ions equals

$$E_{i,kin} = \tfrac{3}{2}kT_i + e_0 V_{bias}. \quad (9)$$

The contributions of positive and negative ions as well as of the electrons and the distribution between these striking particles in respect to the energy transfer depends strongly on the substrate bias voltage which consists of the external substrate voltage V_S and the plasma potential V_{pl}, see Eq. (8). For highly negative voltages only the positive ions determine the influence of the charge carriers, whereas electrons and/or negative ions have to be considered in the case of $V_{bias} \geqslant 0$. It should be emphasized again that the expression of Eq. (9) is applicable in most cases of plasma processing. However, if the IEDF for the ions near the substrate is much more complex the assumption of eV_{bias} for the kinetic energy fails. By considering this fact one has to integrate over the ion energy distribution function $f(V)$ from zero up to the bias potential V_{bias} in order to obtain the mean kinetic ion energy:

$$E_{i,kin} = \int_0^{V_{bias}} f(V) V \, \mathrm{d}V. \quad (10)$$

Furthermore, the thermal energy of the ions (kT_i) can be neglected compared to the directed kinetic energy in non-isothermal plasma process applications because the ions are nearly at room temperature. In high-temperature isothermal plasmas and at high pressures this assumption is not valid and the gradient between ion temperature and substrate temperature has to be taken into account for the determination of the energy influx by ions [42].

The transfer mechanism of the kinetic energy itself is determined by collision processes. Only a part of kinetic energy ($E_{i,kin}^{trans}$) will be transferred to the substrate which depends on the mass ratio of the colliding particles (M_1, M_2), the angle of incidence (Θ), and the energy transfer coefficient (k_c) [30]:

$$E_{i,kin}^{trans} = 4k_c \frac{M_1 M_2}{(M_1 + M_2)^2} E_{i,kin} (\sin \Theta/2)^2 \approx k_c E_{i,kin} (\sin \Theta/2)^2. \quad (11)$$

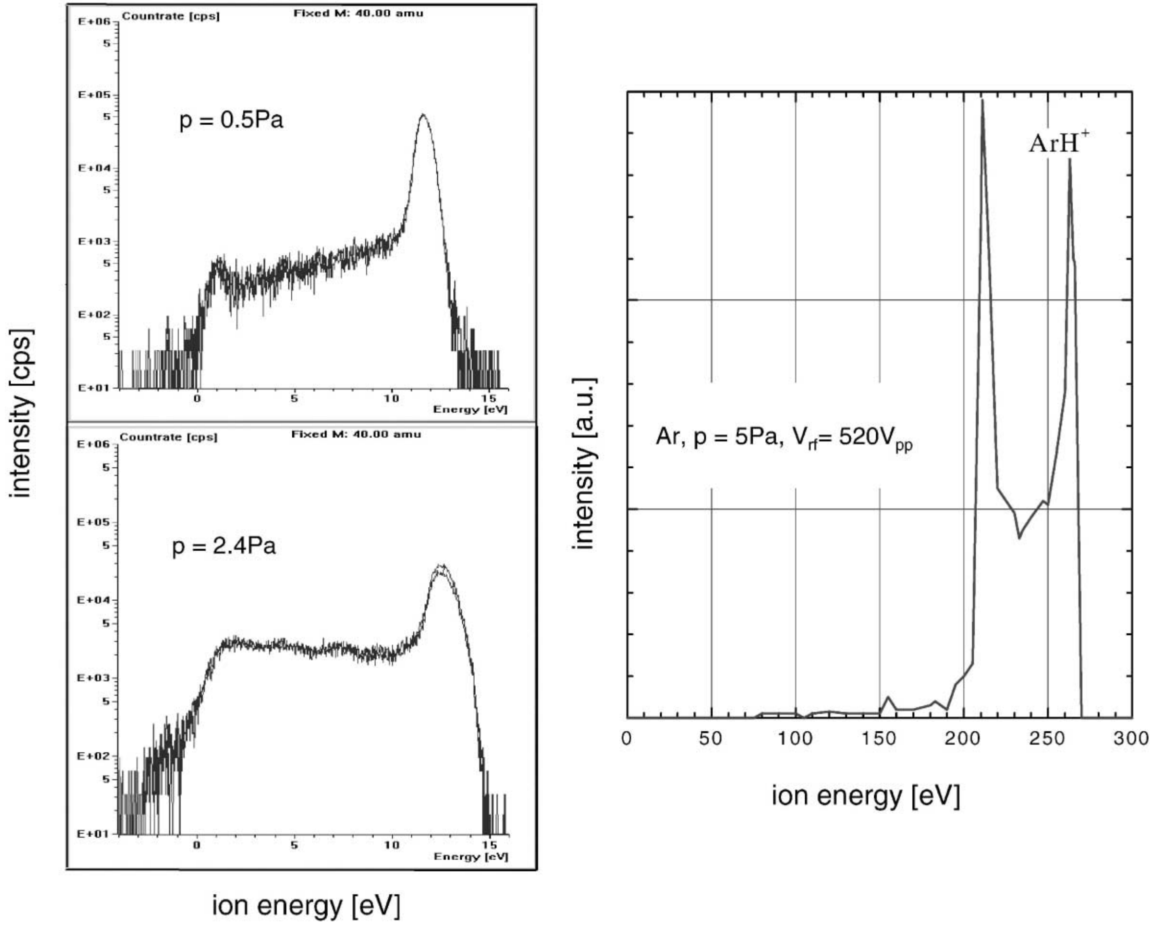

Fig. 2. Left: Influence of pressure on IEDF for an Ar RF plasma. The ions are extracted from $V_{pl} \approx 15\,\text{V}$ to a grounded substrate. Right: IEDF which consists of only the high-energy saddle shaped structure caused by ions passing the plasma sheath without collisions, after [37]. The IEDF is obtained at the powered electrode.

The kinetic transfer coefficient k_c is equal to unity for binary collisions and ranges from 0 to 0.7 for collision cascades of the incoming ions with the solid [30]. Subsequently, under the assumption that all incident ions at the surface of a metal or semiconductor are neutralized, we have for the energy transfer to the substrate:

$$\begin{aligned} J_i &= j_i(E_{i,pot} + E_{i,kin}^{trans}) \\ &= j_i(E_{ion} - \Phi - \gamma_i(\Phi + E_{i,kin})) \\ &\quad + 4k_c \frac{M_1 M_2}{(M_1 + M_2)^2}\left(\frac{3}{2}kT_i + e_0 V_{bias}\right)(\sin\Theta/2)^2. \end{aligned} \tag{12}$$

For low ion temperature T_i and for small γ_i and $E_{ion} \gg \Phi$ as in the case for sputtering one obtains for J_i:

$$J_i = j_i(E_{ion} + \delta e_0 V_{bias}), \tag{13}$$

where $\delta = 4k_c M_1 M_2/(M_1 + M_2)^2(\sin\Theta/2)^2$. For instance, at sputtering of molybdenum the factor δ which describes the efficiency of energy transfer by ions to the substrate has been obtained as 0.5 [30].

As mentioned above, the ion particle flux density j_i (in $\text{m}^{-2}\text{s}^{-1}$) is strongly influenced by the discharge regime and can be described by the

following expressions:

$$j_i = \begin{cases} n_e\sqrt{\dfrac{kT_e}{m_i}}\exp(-0.5) & \textit{BOHM—flux of ions}, \\ \dfrac{4}{9}\dfrac{\varepsilon_0}{e_0}\sqrt{\dfrac{e_0}{m_i}}\dfrac{V_{sh}^{3/2}}{d_{sh}^2} & \textit{ion flux without collisions (CHILD)}, \\ \dfrac{1}{4}n_i v_i & \textit{thermal flux of ions}, \\ n_i v_{amb} & \textit{ambipolar diffusion of ions}. \end{cases} \quad (14)$$

(m_i the mass of ions, T_e the electron temperature, n_e the electron density, n_i the ion density, d_{sh} the sheath width, v_i, v_{amb} are the ion velocities, e_0 the electron charge, ε_0 the electric permitivity constant.)

Although the general equation $j_i = \frac{1}{4}n_i v_i$ is always valid, this expression is hardly applicable because of the complexity of the ion velocity distribution. Under low-pressure conditions ($p \leqslant 10\,\mathrm{Pa}$) the Bohm equation and at very low pressure ($p \leqslant 1\,\mathrm{Pa}$) the Child law are more applicable, respectively.

The Bohm equation yields the ion flux by knowing the electron density which equals the ion density at the sheath edge. Under the idealized assumption of a collisionless sheath this equation results in the same value for j_i as the Child law [43].

The plasma parameters in front of the substrate can be determined experimentally by means of Langmuir probes placed near the substrate or by means of theoretical models. The mean energy of the electrons kT_e and the plasma potential V_{pl} can be derived from the second derivative of the probe characteristic [44]. In the theoretical interpretation of the probe characteristic, one has carefully to take into account the RF compensation of the probe and the presence of negative ions (for example [45]) and/or of magnetic fields (for example [46]), if such disturbing effects are important. In [36] for an RF plasma a relation between the macroscopic discharge power and the ion flux density is given on the basis of a simplified total power balance and under the assumption that the time-averaged ion and electron fluxes are equal in order to maintain quasi-neutrality. By means of such relations between macroscopic and internal quantities it is possible to achieve an independent control of ion energy and ion flux which is suitable for the control of material properties in plasma processing. Investigations on the total ion flux and the mean ion energy at different pressure and various RF power in an inductively coupled argon plasma have shown that the energy flux density mainly depends on the supplied power and only less on the pressure [47]. This behavior is due to the following dependencies: at a constant pressure the ion flux j_i increases with increasing power (Fig. 3), while the mean kinetic ion energy $E_{i,kin}$ at constant power decreases with increasing gas pressure (Fig. 4). Hence, the energy flux density of the ions which is the product of both seems to be a suitable quantity to describe the energetic conditions on the substrate surface in different equipments and under different discharge conditions.

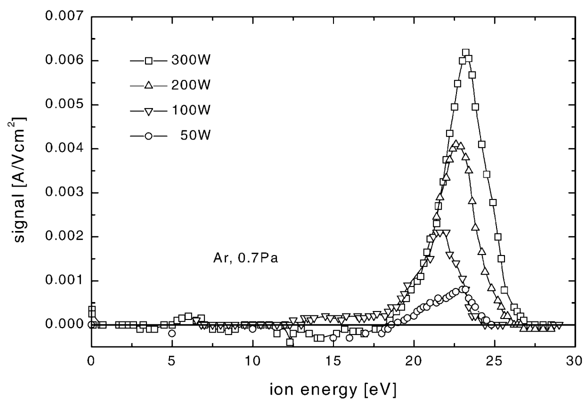

Fig. 3. Ion energy distribution in dependence on RF power for constant pressure, measured by Woodworth et al. [47]. The ion flux increases while the mean ion energy is nearly independent on RF power.

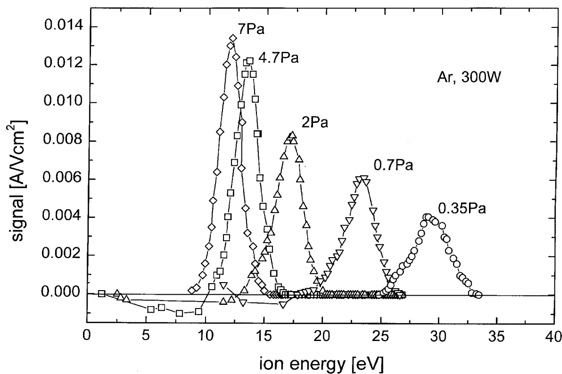

Fig. 4. Ion energy distribution in dependence on gas pressure for constant RF power, measured by Woodworth et al. [47]. The mean ion energy decreases with increasing pressure due to collisions.

The considerations given so far are concerned to positive ions. However, in a variety of process plasmas (e.g. etching) which contain electronegative species as SF_6, O_2, Cl_2, etc. a large amount of negative ions occurs. In such plasmas the negative ion density n_{i-} may be even comparable to the electron density n_e [48]. Although the presence of negative ions influences the discharge characteristics as well as the internal plasma parameters and their energy distribution, they are almost negligible in regard to the energy flux towards a substrate — as long as it is at ground, floating or negative bias potential which is mostly the case in plasma processing. Because of the negative substrate potential in respect to the plasma and the surrounding sheath, the negative ions are efficiently trapped in the plasma bulk and even in RF discharges they cannot reach the substrate in a considerable number due to their large mass.

The situation for electrons is quite different because of their essentially smaller mass and the more complex energy distribution.

Energy influx by electrons (J_e). An exact description of the electron behavior in a non-isothermal gas discharge requires the knowledge of the electron energy distribution function (EEDF) which can be determined by Langmuir-probe measurements, see for instance [49,50]. Fig. 5 shows an example for the second derivative of the probe current which is a measure for the

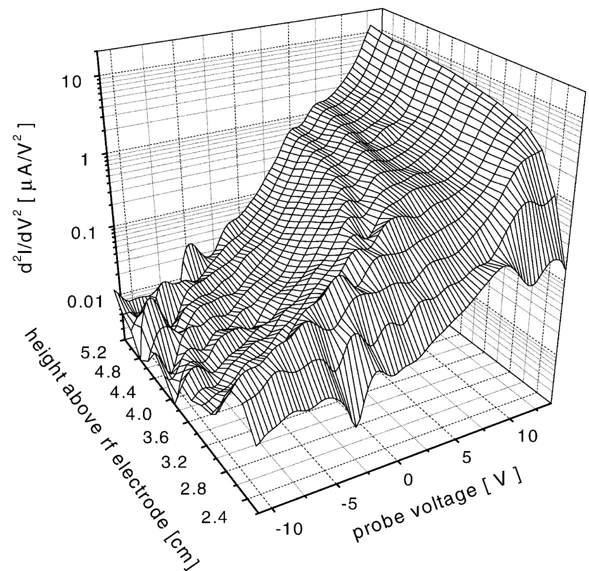

Fig. 5. The second derivative of Langmuir-probe characteristics, which is a measure for the EEDF obtained at different heights above the RF electrode [51], ($P = 0.75\,\mathrm{Pa}$, $P = 10\,\mathrm{W}$).

electron energy distribution function. The distributions have been obtained for an argon RF plasma at different heights above the powered electrode [51]. Calculations of EEDF are based on the solution of the Boltzmann equation [52] or by theoretical simulations concerning Monte-Carlo [53] and particle-in-cell methods [54].

One has to distinguish between an isotropic part $f_0(E)$ and an anisotropic part $f_1(E)$ of the EEDF which lead to different information on the electron component of the plasma. By means of the isotropic part one obtains information on the electron density n_e and the mean energy kT_e, while $f_1(E)$ yields the directed electron flux j_e. The isotropic component can be measured by cylindrical probes, whereas angular-resolved planar probes are used for the determination of the latter component.

In some cases it is possible to model the EEDF by means of standard distributions, for example Maxwell or Druyvesteyn distribution. In Fig. 6, both distributions are presented schematically. Comparing the most common standard distribution functions, there is a significant difference in their high-energy tails. In Fig. 7, the contribution

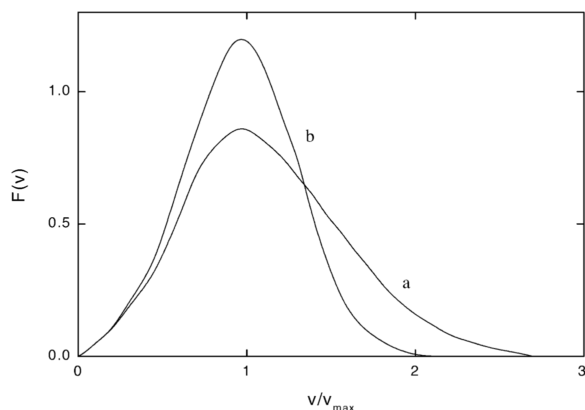

Fig. 6. Comparison of electron velocity distribution functions $F(v)$ (schematic): (a) Maxwell, (b) Druyvesteyn (v the velocity, v_{max} the velocity at the maximum).

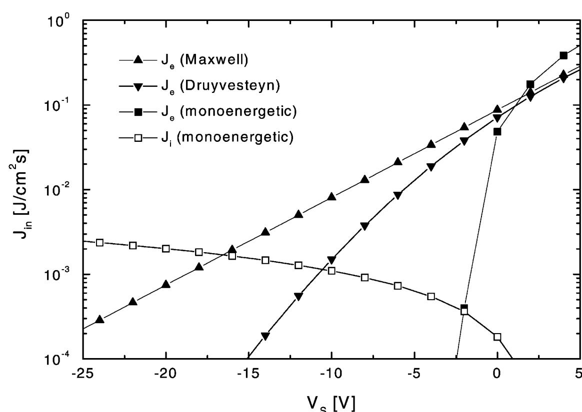

Fig. 7. Calculated energy flux of electrons (J_e) and ions (J_{i+}) in dependence on substrate potential for different EEDFs, from [55]. (RF plasma in argon, $n_e = 3 \times 10^9\,\mathrm{cm}^{-3}$, $kT_e = 4.2\,\mathrm{eV}$, $V_{pl} = 1\,\mathrm{V}$).

of electrons J_e for the two energy distribution functions is plotted for typical glow discharge values [55].

In order to reach the substrate surface the electrons have to overcome the bias voltage V_{bias} in front of the substrate, which consists, as already mentioned, of the external substrate voltage V_S and the plasma potential V_{pl}, see Eq. (8). The energy flux J_e due to the plasma electrons arises from the integration over the EEDF from V_{bias} up to infinity which yields for a Maxwellian EEDF:

$$J_e = n_e \sqrt{\frac{kT_e}{2\pi m_e}} \exp\left(\frac{-e_0 V_{bias}}{kT_e}\right) 2kT_e = j_e E_e. \tag{15}$$

By comparison of the terms one can identify the energy of the plasma electrons as

$$E_e = \int_{V_{bias}}^{\infty} f(E) E \,\mathrm{d}E = 2kT_e \tag{16}$$

and the electron flux density of the plasma electrons j_e can be expressed by

$$j_e = n_e \sqrt{\frac{kT_e}{2\pi m_e}} \exp\left(\frac{-e_0 V_{bias}}{kT_e}\right). \tag{17}$$

In the special case of highly mono-energetic electrons the expression for E_e becomes

$$E_e = e_0(V_{cat} - V_{bias}) \tag{18}$$

with V_{cat} being the negative cathode potential. Generally, these high energetic electrons are not detected by electrostatic probe measurements.

An analysis of the charged components of the plasma by using the general Eqs. (5)–(18) listed above will in principle yield the part of surface heating caused by ions and electrons. Although several heat sources act together, e.g. radiation, chemical reactions, neutrals and charge carriers, it may be possible to separate the contribution of the charge carriers by variation of the bias potential.

2.1.3. Energy influx by neutral species (J_n)

In addition to charge carriers, neutrals of the background gas as well as neutrals of the process components (e.g. deposition material, etch products, radicals, etc.) interact with the substrates in plasma processing of solid surfaces and, hence, contribute to the thermal power balance.

The potential energy of neutral species in a plasma is distributed between vibration, rotation, dissociation and electronically excited states (metastables), while the kinetic energy arises only from the translation.

In general, the following components may contribute to the energy transfer by neutrals in commonly used plasma process applications at low pressure:

- heat of adsorption: J_{ads} or condensation: J_c, respectively,
- excitation energy (vibration, rotation, metastables): J_*,
- kinetic energy of sputtered or scattered particles from the cathode: $J_{n,sput}$,
- energetic neutrals of the process gas ($J_{n,kin}$) which may originate from charge exchange mechanisms.

The first two components represent the most important transfer channels of potential energy. A short review on the different kinds of potential energy transfer mechanisms of the excitation modes may be found in [18,56].

Adsorption and condensation (J_{ads}, J_c). In most relevant process plasmas the adsorption of neutral species is of importance. In an adsorbed state (see Fig. 8) the adsorption heat E_{ads} is released, which results in heating the surface. The input J_{ads} by the adsorption is given by

$$J_{ads} = j_n \gamma E_{ads}, \tag{19}$$

where j_n describes the flux of neutrals and γ denotes the sticking coefficient.

The initial sticking coefficient γ may consist of two contributions with a precursor-mediated sticking probability of physisorption (γ_p) and a direct sticking probability of chemisorption (γ_c) [57]. Fig. 8 shows the potential energy curve for molecular sticking. There is an activation barrier (E_a) between the physisorption well and the chemisorption well. Since the probability of physisorption is influenced by the surface temperature and the probability of chemisorption depends strongly on the kinetic energy of the incoming molecule in order to overcome the activation barrier, the sticking coefficient γ should exhibit a dependence of both quantities.

Fig. 9 illustrates both dependencies for the sticking of Cl_2 on silicon measured in a pulsed molecular-beam machine [57]. Several values of sticking coefficients for typical sample/surface systems may be found in [58].

A macroscopic phenomenon of adsorption is condensation. Especially in the case of thermal evaporation or sputtering of metallic films this part can become important [14,16]. The contribution J_c to the thermal power input due to condensation of metal vapor can be estimated by [59]

$$J_c = q_c \varrho R \sim \gamma_n j_n E_B, \tag{20}$$

where q_c is the specific condensation heat of the vapor, ϱ is the mass density of the growing layer and R marks the deposition rate. In a microscopic picture the condensation J_c can also be approximated by the product of the condensing particle flux j_n, the sticking probability γ_n of the species and the binding energy E_B.

Metastables (J_*). The flux of metastables can be estimated by knowing the concentration n_* and the local density gradient of the excited particles.

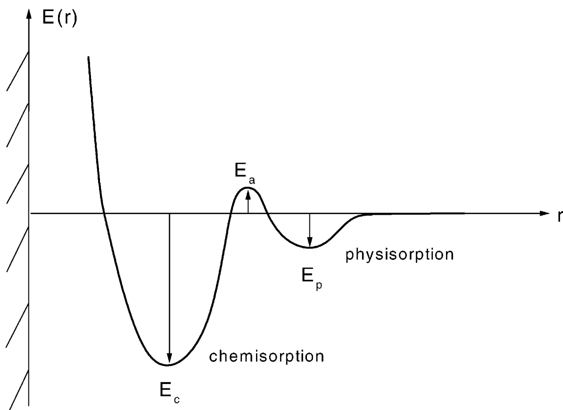

Fig. 8. Schematic illustration of the potential energy curve for the sticking model of a molecule.

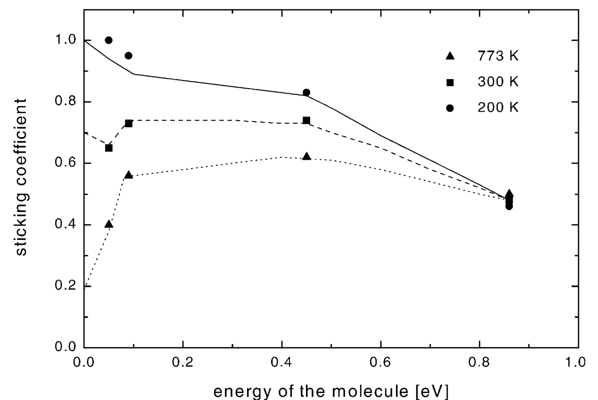

Fig. 9. Sticking coefficient γ versus energy of incident Cl_2 molecules for different surface temperatures, from [57].

These quantities can be determined by optical methods as absorption spectroscopy [60] and laser-induced fluorescence (LIF) [61]. Consequently, by knowing the energy of a metastable (E_*), the amount of power (J_*) resulting from particle excitation can be obtained.

The component of heating of a surface by resonance excited states and metastable states has been discussed in more detail, for example, in [26]. The authors obtained the density n_* of the metastables in an Ar plasma by a steady-state particle balance equation which includes the production of metastables through electron-impact excitation and the loss through ionization, quenching and diffusion loss to the walls. As described in [26] the energy flux due to bombardment by excited states can be written as

$$J_* = \xi_* n_* \sqrt{\frac{8kT_g}{\pi m}} E_*, \tag{21}$$

where ξ_* is the probability of energy transfer to the surface and the metastable states are at the neutral gas temperature T_g. The transfer coefficient ξ_* depends strongly on surface material. For catalytically active surfaces (metals) it can reach 0.1–1, while for amorphous oxides and ceramics $\xi_* \approx 10^{-5}$ [62].

However, the rather rare information on metastable influence on surface heating in plasma–wall interaction at low pressure yields to the conclusion that this contribution is negligible in comparison to the other parts. This conclusion is also supported by the estimated J_* values in [26] which are less than 1% in comparison to the influence of charge carriers and even of plasma radiation.

Kinetic energy of sputtered particles ($J_{n,sput}$). The contribution of neutrals to the total power balance plays an important role, for instance, in sputtering processes which are essentially influenced by the potential distribution between cathode (target), plasma and substrate. The neutral particles sputtered from the target having kinetic energies of $\approx$1–30 eV may transfer a considerable amount of their kinetic energy to the substrate. Related theories [28,63] and TRIM simulations [64] show that the energy distribution of the sputtered neutrals is close to $U_B/2$, where U_B is the surface binding energy of the atoms in the sputter target. Depending on the gas pressure, the sputtered particle lose some part of their kinetic energy via collisions with the gas atoms and become partially thermalized on their way to the substrate.

Kinetic energy of neutrals of the process gas ($J_{n,kin}$). In addition to the kinetic energy of the sputtered target atoms, there is also a kinetic energy input via highly energetic neutral gas atoms, which are produced by neutralization of backscattered ions [28]. Neutrals have a low scattering cross section with the background gas and impinge on the substrate with energies close to the initial value.

Fast neutrals are also produced by charge exchange of accelerated ions with neutrals in the plasma sheath [38]. Collisions in the sheath are important when the mean free path of the ions is less than the sheath thickness. This is the case for pressures higher than about 1 Pa. Ion-neutral collisions have a strong influence on the ion and neutral dynamics. Resonant charge exchange collisions for atomic ions have a large exchange cross section in the order of $10^{-15}\,\mathrm{cm}^2$. Such a collision generates a thermal ion and a fast neutral by the exchange of an electron. The non-resonant charge transfer proceeds via momentum transfer where the energy of the colliding ion is distributed due to the energy and momentum conservation laws.

The related energy input $J_{n,kin}$ is

$$J_{n,kin} = k_n j_n E_{n,kin}, \tag{22}$$

where $E_{n,kin}$ is the kinetic energy of a fast neutral and k_n a factor which expresses the energy transfer efficiency similar to ions, see Eq. (11). The flux j_n of fast neutrals is obtained directly from the gas temperature T_g. The latter can be estimated by considering the gas heating and cooling processes in the chamber. In a low-pressure glow discharge, gas heating is mainly provided by electron–atom elastic collisions and as already mentioned by ion–atom charge exchange collisions.

At high gas pressures and for large temperature differences between substrate (T_S) and the process gas (T_g), energy transport by neutrals

can proceed via [42]

$$J_{n,kin} = \alpha k_n (T_g - T_S) n_n \sqrt{\frac{kT_g}{2\pi m_n}}, \tag{23}$$

where T_g marks the temperature of the gas and n_n the density of the gas.

A characteristic quantity for the energy exchange is the accomodation coefficient α:

$$\alpha = \frac{(E_{in} - E_f)}{(E_{in} - E_s)}, \tag{24}$$

where E_{in} and E_f are the initial and final energy of the plasma species and E_s is the thermal energy per atom of the substrate surface. The accomodation coefficient α is always less than unity and depends strongly on the nature of the colliding particles and the surface. Besides translational energy transfer for molecules also vibrational and rotational energy transfer is important. For more information on this contribution and their relations, see for instance [65,76].

Applications where the substrate heating by energetic neutrals dominates are, for example, magnetron discharge sputtering [50], thermal evaporation and expanding arc plasmas [66].

As an illlustration for the influence of the different energetic contributions as radiation, charge carriers, and fast neutrals which have been described above, experimental studies on magnetron sputtering as a typical plasma process will be given in the following. Those processes have been extensively studied, for example, in [16,28,29].

An experimental and theoretical study of sputtering of molybdenum in an argon DC-magnetron discharge was carried out by Andritschky et al. [28]. They assumed that energy and momentum of the deposited metal atoms and ions are the determining factors during film deposition. With increasing gas pressure the energy deposited by sputtered particles decreased because of thermalization while the other contributions remained almost constant, see Fig. 10. At constant pressure and increasing negative bias voltage, the power transported via ion bombardment becomes dominant (Fig. 10). Both energy and momentum transfer of the particles have been found to influence crystal structure, density, and intrinsic stress of the growing molybdenum film.

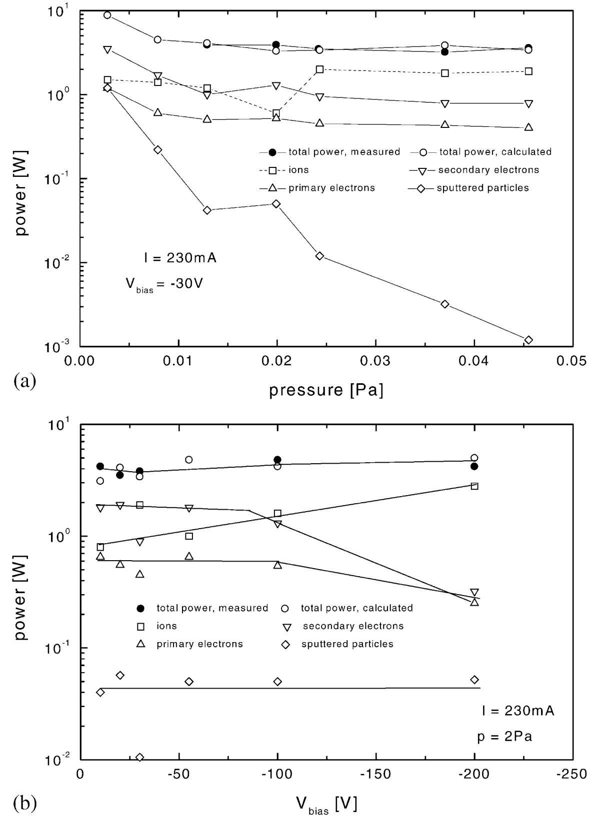

Fig. 10. Power transported via particle bombardment to the substrate at Mo sputtering versus gas pressure, and power transported via particle bombardment to the substrate at Mo sputtering versus bias voltage, after [28].

One of the very first investigations on substrate heating in cylindrical magnetron sputtering has been carried out by Thornton [16]. In this study, energy fluxes were examined for different discharge conditions where the following parameters have been varied: axial magnetic field (0.01–0.02 T), current densities (30–120 A m^{-2}), discharge voltage (500–1000 V), Ar gas pressure (0.13–1.3 Pa), and cathode material. The energy per deposited metal atom, shown in Table 1, has been examined for several metals.

Wendt et al. [29] examined the thermal power at the substrate for magnetron sputtering of ZnO for a DC and RF discharge at 50 W and 0.8 Pa. They measured a twice as large heating flux for the RF compared to the DC discharge mode. This difference was mainly due to the much higher

Table 1
Heating fluxes per atom for argon sputtering with cylindrical magnetron for several cathode materials, from [16]

Metal	Atomic mass	Heat of condensation ($eV\,atom^{-1}$)	Average kinetic energy of the sputtered atoms ($eV\,atom^{-1}$)	Plasma radiation ($eV\,atom^{-1}$)	Estimated flux heating ($eV\,atom^{-1}$)	Measured heating ($eV\,atom^{-1}$)
Al	27.0	3.33	6	4	13	13
Ti	47.9	4.86	8	9	22	20
V	50.9	5.29	7	8	20	19
Cr	52.0	4.11	8	4	16	20
Fe	55.8	2.26	9	4	15	21
Ni	58.7	4.45	11	4	19	15
Cu	63.5	3.50	6	2	12	17
Zr	91.2	6.34	13	7	26	41
Nb	92.9	6.50	13	8	28	28
Mo	95.9	6.88	13	6	26	47
Rh	102.9	5.60	13	4	23	43
Cd	112.4	1.16	4	1	6	8
In	114.8	2.52	4	2	9	20
Hf	178.4	6.33	20	7	33	63
Ta	181.0	8.10	21	9	38	68
W	183.8	8.80	22	9	40	73
Au	197.0	3.92	13	2	19	23

contribution of the Ar^+ ions from the plasma. The results are compared in Table 2.

Table 2
Thermal power (P/A) at the substrate for a DC and RF sputtering discharge at 50 W and 0.8 Pa, from [29]

Particles	P/A (mW/cm^{-2}) DC	P/A (mW/cm^{-2}) RF
Positive ions (Ar^+) from the plasma	5.3	23.2
Electrons from the plasma	1.9	5.5
Zn, O from the target	2.3	0.7
Sum	9.5	29.4
Measured	15.6	32.0

2.1.4. Energy influx by exothermic chemical reactions ($J_{react,1}$)

Evidence for substrate heating by exothermic reactions on the processed surface has been reported, for example, with respect to plasma etching of silicon with fluorine containing compounds [67] and during plasma cleaning of contaminated metal surfaces [68].

If the formation of product molecules is an exothermic process, which takes place in the presence of a third collision partner, e.g. a solid surface, this process will contribute to substrate heating. The product molecules may desorb at the electronic ground state, but with internal excitation of vibration or rotation. Thus, there is a varying part of the reaction energy transferred between the solid surface and the desorbed molecule. The latter part is used as desorption energy.

In the case of molecular recombination as a special surface reaction process, the fraction of the energy transferred to the solid has been described by Halpern and Rosner [69] on the basis of mass and energy balance considerations. The percentage of the association energy which is used for surface heating varies with the chemical composition of the surface.

Concerning the association of atoms on a solid surface one has to distinguish between two basic mechanisms [69–71]. In the case of the Langmuir–Hinshelwood mechanism two adsorbed atoms recombine to a resulting product molecule removing an energy equal to the activation energy of molecular desorption [70]. For the Eley–Rideal

mechanism a molecule is generated by gas phase atom impact onto an adsorbed atom [71]. A Eley–Rideal-produced molecule may immediately escape or remain physisorbed for a residence time during which it may deposit some part of its energy.

2.2. Energy loss processes

From a general point of view and similar to the energy input, the heat loss $\dot{Q}_{out}$ of the substrate during plasma processing consist of the following terms:

$$\dot{Q}_{out} = \int (J_{rad,2} + J_{ext,2} + J_{des} + J_{react,2} + J_{particle})\,\mathrm{d}A. \tag{25}$$

- energy $J_{rad,2}$ radiated from the substrate at temperature T_S, which includes contributions of both the front side in direction of the plasma and the back side of the substrate in direction of the holder,
- heat loss $J_{ext,2}$ by external cooling, i.e. the energy transport by conduction along the substrate holder and by convection of the surrounding gas,
- energy sink J_{des} due to desorption of particles into the gas phase and diffusion into the solid bulk,
- energy $J_{react,2}$ concerning endothermic chemical reactions at the surface including dissociation,
- energy transport $J_{particle}$ from the substrate due to sputtering of surface atoms and secondary electron emission.

2.2.1. Radiation ($J_{rad,2}$)

In most cases a non-negligible part of the substrate heat flows via thermal radiation. This is especially the case for processes where the substrate temperature is comparatively high (e.g. CVD) and/or if the pressure is very low for convection (e.g. electron beam evaporation). Also in applications where only a poor contact between hot substrate and cold holder is realized and, therefore, conduction along the sample support is small, radiation is one of the most important losses.

The power dissipated by radiation from the substrate can be determined from Stefan's law as

$$\int J_{rad,2}\,\mathrm{d}A = A_S \sigma(\varepsilon_S T_S^4 - \varepsilon_{env} T_{env}^4), \tag{26}$$

where ε_S, ε_{env} are the emissivity of the substrate surface and the environment, respectively, A_S the emitting area of the substrate (front and back side), σ the Stefan–Boltzmann constant, T_S the substrate surface temperature, T_{env} the environmental temperature (reactor walls, etc.). The ε values are total hemispherical emissivities and mostly it is assumed that $\varepsilon_{env} \approx 1$, while the emissivity of the substrate (ε_S) is dependent on the material. Typical values for metals as Al, Cu, Ni are 0.02–0.1, for pyrex we find 0.8, and for glass, ceramics, carbon ε_S is in the order of 0.9 [31]. During the plasma process and, hence, due to substrate heating the substrate emissivity may vary by a few per cent and the environmental temperature T_{env} unlikely to be precisely constant. But the usually small variations in these terms are ignored.

The energy balance of substrates during CVD and PECVD has been studied by several authors, see for instance [15,23,72].

2.2.2. Conduction and convection ($J_{ext,2}$)

The heat losses by external cooling of the substrate ($J_{ext,2}$) consist of heat conduction by the surrounding gas ($J_{cond,gas}$) and heat conduction along the solid sample holder ($J_{cond,solid}$):

$$J_{ext,2} = J_{cond,solid} + J_{cond,gas}. \tag{27}$$

The effect of gas pressure on substrate cooling has been demonstrated in [43], see Fig. 11. Usually, compared to the other energy loss processes the convection by the gas has only a small influence because of the low gas density. But in some applications, the substrate can be cooled by conduction through the gas between its back side and the cooled susceptor [72]. This procedure is widely used in semiconductor industry by creating a He pressure of a few millibar between the substrate and the support.

Following Fouriers law of heat conduction, the power loss along the substrate holder is

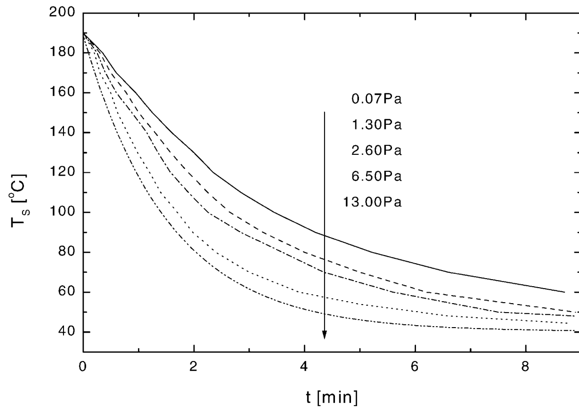

Fig. 11. Cooling of a substrate in argon after the plasma is switched off for different gas pressure, from [43].

given by

$$\int J_{cond,solid}\,\mathrm{d}A = \frac{1}{R_{th}}(T_S - T_H) = \frac{\lambda_S A_S}{d_S}(T_S - T_H). \tag{28}$$

(T_S the temperature of the substrate, T_H the temperature of the sample holder, R_{th} the equivalent thermal resistance, λ_S the heat conductivity of the substrate and support, d_S, A_S are the length and cross section of the conductor.)

In order to determine the substrate cooling by thermal conduction due to gas atoms striking the surface one has to distinguish between the collisional regime and the free molecular regime [42,43,59,26]. In the collisional regime where the mean free path $\bar{\lambda}$ of the gas is much smaller than the boundary sheath d_{sh} the heat flux density is proportional to the local gradient of temperature:

$$\int J_{cond,gas}\,\mathrm{d}A = N_u \lambda_g \frac{(T_S - T_g)}{d_{sh}}. \tag{29}$$

(N_u the Nusselt number, λ_g the thermal conductivity of the gas ($1.6 \times 10^{-4}\,\mathrm{W\,cm^{-1}\,K^{-1}}$ for Ar), d_{sh} the thickness of the boundary layer in front of the substrate.)

At gas pressures (10^{-2}–10 Pa) which are typical for plasma processing, the free molecular regime is important where the mean free path of a gas atom/molecule is greater or comparable to the sheath thickness ($\bar{\lambda} \geqslant d_{sh}$). In this regime the thermal flux is proportional to the temperature difference between gas temperature T_g and substrate temperature T_S as well as to the free molecular heat conductivity χ and the gas pressure p:

$$\int J_{cond,gas}\,\mathrm{d}A = \alpha\chi p(T_S - T_g)A_S. \tag{30}$$

The accomodation coefficient α has been introduced in Eq. (24) and the free molecular heat conductivity is according to Knudsen theory [73]:

$$\chi = \frac{c_p/c_V + 1}{c_p/c_V - 1}\frac{1}{16\sqrt{T_g}}\sqrt{\frac{8k}{\pi m}}. \tag{31}$$

m marks the mass of the gas atoms and c_p/c_V is the adiabatic coefficient which is for noble gases 5/3 and for molecule gases 7/5.

As shown in [43,72] the increase of the gas flow does not make any sensible change in the substrate temperature under normal operating ranges at low-pressure plasma conditions. Therefore, it can be mostly neglected. However, under conditions of gas/plasma-jets gas flow convection might even be dominant and, hence, the convection can be an important contribution to the energy balance at the substrate surface [74].

2.2.3. Desorption processes (J_{des})

The desorption of atoms/molecules from solid surfaces under vacuum conditions is a process consisting of sequential phenomena of gas transport from inside the solid (bulk diffusion) and of desorption of gas molecules from the surface.

The "first order" desorption rate R_{des} [75,76] from a surface is described by the Frenkel equation:

$$R_{des} = \frac{\mathrm{d}n_{ads}}{\mathrm{d}t} = -\frac{n_{ads}}{\tau_{des}}, \tag{32}$$

where n_{ads} is the number of gas species adsorbed per unit area and τ_{des} is a characteristic time related to the average residence time of the gas species on the surface [77]. The time of residence is related to an activation energy E_{des} by

$$\tau_{des} = \tau_{des0}\exp(E_{des}/kT_S). \tag{33}$$

The pre-exponential factor τ_{des0} is the vibration period of the adsorbed particle, which is in the range of 10^{-12}–10^{-14} s. The activation energy E_{des} on the surface depends mainly on the kind of interaction between the atoms of the solid and the

gas species (e.g. physisorption, chemisorption). It is also influenced by the arrangements (e.g. steric factors, crystal structure of the surface) of the interacting partners. Furthermore, the overall desorption rate R_{des}^{total} from a heterogeneous surface with a continuous desorption energy distribution $f_{des}(E)$ is represented by

$$R_{des}^{total}(T_S, t) = \int f_{des}(E) R_{des}(T_S, t, E)\,\mathrm{d}E, \quad (34)$$

where $R_{des}(T_S, t, E)$ represents the single site desorption introduced above [78].

In order to determine the desorption mechanisms of gas molecules from solid surfaces and, consequently, the characteristic desorption energy, thermal desorption spectroscopy (TDS) is often employed. In TDS diagnostics the surface under investigation is heated within a defined temperature range and with a defined heating rate. The generation rate of the desorbed particles is monitored by a quadrupole mass spectrometer under ultra-high vacuum conditions [79].

Studies on TDS measurements of NH_3 over molybdenum nitride films yield, for instance, desorption energies of 0.95 eV assuming a pre-exponential factor of 10^{-13} s in Eq. (33) [79].

2.2.4. Endothermic chemical processes ($J_{react,2}$)

For the interpretation of surface reactions by plasma–wall interaction a broad arsenal of different physical and chemical mechanisms exists. Besides the ordinary evaporation at elevated temperatures or due to a localized thermal pulse created by laser or incident energetic particle beams, three basic mechanisms have to be taken into account: physical sputtering (PS), chemical sputtering (CS) and surface film reaction (SFR). While physical sputtering is related to the energy loss by impact of energetic particles discussed at the end of this section the latter two processes are frequently endothermic reactions.

In the endothermic chemical sputtering (CS) an incident particle A reacts with a bulk atom B without an intermediate boundary state to a final product AB. The product molecule AB may desorb instantly (direct chemical sputtering) or it remains for a certain residence time (delayed chemical sputtering) at the surface.

Analogous to physical sputtering, the rate R_{CS} for chemical sputtering is proportional to the flow rate j_A of incoming chemically active particles to the surface:

$$R_{CS} = \varepsilon_{CS} j_A, \quad (35)$$

where ε_{CS} denotes the coefficient of gasification which describes the surface reaction probability with the incident species. According to the mechanism of activated chemical reactions ε_{CS} represents the probability for the appearance of particle energies above a certain limit E_{CS} resulting in an exponential dependence

$$\varepsilon_{CS} = \varepsilon_{CS0} \exp(-E_{CS}/kT_S). \quad (36)$$

The Arrhenius behavior with only a single activation energy is applicable for direct chemical sputtering in the case where both the solid surface and the incoming particles are characterized by the same temperature. If there are different temperatures or a monoenergetic particle beam (e.g. energetic ion beam) more complicate dependencies must be considered.

The resulting energy loss $J_{react,2}$ by this reaction may be given as

$$J_{react,2} = R_{CS} E_{CS}. \quad (37)$$

In contrast to chemical sputtering, in the case of surface film reaction (SFR) the incoming particles A are adsorbed at the surface prior to the chemical reaction. The desorption rate R_{SFR} then depends primary on the degree of coverage Θ with adsorbed particles:

$$R_{SFR} = k_{SFR} n_0^2 \Theta \quad \text{with } \Theta = n_{ads}/n_0, \quad (38)$$

where n_{ads} the number of adsorbed atoms A per unit area, n_0 the total number of substrate surface sites per unit area of the substrate.

At full coverage the temperature dependence of R_{SFR} is governed by $k_{SFR}(T_S)$ which again shows an Arrhenius-type behavior:

$$k_{SFR} = k_{SFR0} \exp(-E_{SFR}/kT_S). \quad (39)$$

However, with incomplete coverage a more complex dependence of $R_{SFR}(T_S)$ holds [3]. If the surface film reaction dominates $J_{react,2}$ is given by

$$J_{react,2} = R_{SFR} E_{SFR}. \quad (40)$$

Chemical sputtering (CS) and surface film reaction (SFR) are the two limiting cases with many transitions between them. In Section 4.2.1 some examples for temperature dependencies of plasma etching are discussed in more detail. An overview on basic mechanisms in plasma etching and typical values for different technological etching systems are given in [3].

2.2.5. Physical sputtering of surface atoms and secondary electron emission ($J_{particle}$)

Another energy loss process at substrate surfaces is due to those particles which are released from the surface by physical sputtering (J_{PS}) and by emission of secondary electrons ($J_{\gamma,el}$):

$$J_{particle} = J_{PS} + J_{\gamma,el}. \tag{41}$$

In contrast to losses by desorption or chemical reactions, these particle losses are caused by the impact of energetic ions or neutrals at the substrate. However, this contribution is in many technological plasma processes relatively small because the potential drop between plasma and substrate is mostly much less than 100 eV.

For both sputtering of substrate surface atoms and emission of secondary electrons a threshold energy is required. The threshold values depend on the mass ratio of the colliding partners, the binding energy, the surface coverage of adsorbed atoms, etc. Above the threshold value the yield, e.g. the number of ejected particles per incident ion, shows a characteristic energy dependence [123]. In Fig. 12, examples for the energy dependence of the sputter yield are presented, while energy distributions of ejected atoms and electrons, respectively, are shown in Figs. 13 and 14 [80,81]. The energy distribution of sputtered particles can be described by the Thompson formula [80], where a planar surface potential U_B is assumed and which has to be overcome by the sputtered surface atoms:

$$\frac{d^2 Y}{dE\, d\beta} \sim \frac{E}{(E + U_B)} \cos \beta. \tag{42}$$

The energy distribution of the sputtered particle yield (dY/dE) has a maximum at about $(1/2)U_B$ and falls off at high energies as $1/E^2$ until the transferable energy is reached. A summary of typical values for different plasma process systems concerning physical sputtering may be found in [63,80].

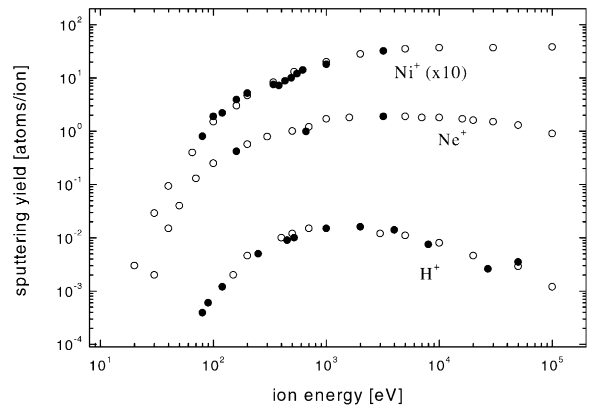

Fig. 12. Dependence of the sputtering yield of Ni on the energy of different incident ions, from [123]. Full symbols: calculated data (TRIM.SP), open symbols: measured data.

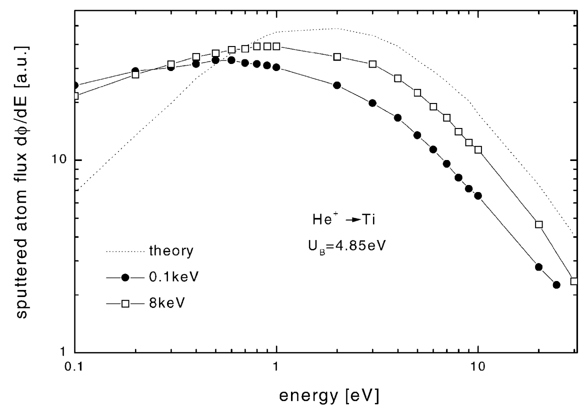

Fig. 13. Energy distribution of particles ejected by physical sputtering of Ti by He-ions. Comparison of measurements and Thompson-model, from [80].

The secondary electron yield as it was observed in [81] showed a strong dependence on the amount of adsorbed gases and increased in an approximately linear manner with the coverage. The kinetic energy distributions were almost insensitive to impact energy, while the ejection probability increased with increasing impact energy above a threshold of about 50 eV.

Summarizing, the energy loss of a substrate by particle emission depends strongly on the energy of the hitting particles originating from the plasma

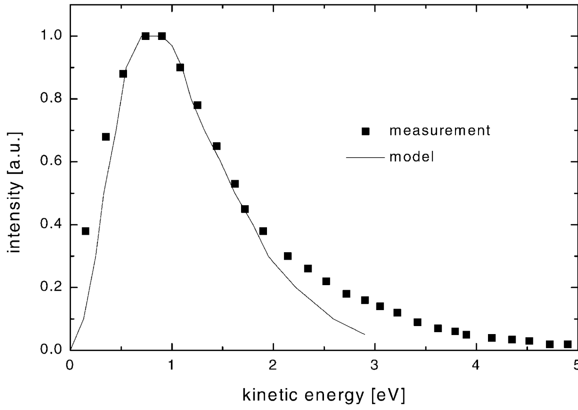

Fig. 14. Kinetic energy spectra for secondary electrons released at sputtering of Al by a Na^+ ion beam, from [81].

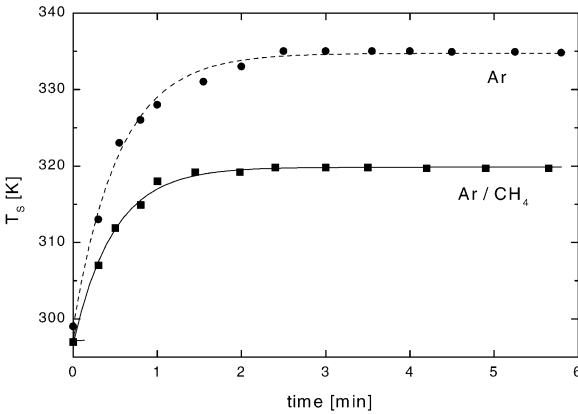

Fig. 15. Examples for measured time-dependent temperature curves. Glass substrates were heated by a cascaded arc discharge of Ar and Ar/CF_4, respectively, from [66]. ($p = 40\,\text{Pa}$, $P = 4.2\,\text{kW}$).

which is dissipated to a large extent in the surface-near region and, hence, the loss is typically rather small.

3. Experimental determination of thermal quantities

When a solid comes into contact with a plasma, energy transfer takes place. The substrate is heated and, after a certain time, it reaches a thermal equilibrium state as, for example, shown in Fig. 15. This steady state is determined by a balance of energy gain from the plasma processes and energy losses by conduction, radiation, etc. [14–17,20,82].

The general power balance at the surface is given by

$$\dot{Q}_{in} = \dot{Q}_S + \dot{Q}_{out}, \tag{43}$$

where $\dot{Q}_{in}$ is the total heat flux towards the substrate (energy input), $\dot{Q}_{out}$ is the heat flux from the substrate (energy output) and $\dot{Q}_S$ denotes the transferred power that heats the substrate,

$$\dot{Q}_S = \frac{\mathrm{d}}{\mathrm{d}t}(m_S c_S T_S) = \varrho_S d_S A_S c_S \left(\frac{\mathrm{d}T_S}{\mathrm{d}t}\right). \tag{44}$$

(m_S the mass, c_S the specific heat capacity, ϱ_S the mass density, d_S the thickness, A_S the area, T_S the surface temperature of the substrate, respectively.)

3.1. Heat flux measurements

By using the substrate as a calorimeter probe the integral heat flux can be obtained by evaluation of the temperature curves, e.g. Fig. 15.

The energy flux from the substrate $\dot{Q}_{out}$ consists of heat conduction by the gas, the heat conduction along the sample holder, and radiation:

$$\begin{aligned}\dot{Q}_{out} &= \alpha\chi p(T_S = T_{env})A_S \\ &\quad + \frac{\lambda_S}{d_S}A_S(T_S - T_H) \\ &\quad + 2\sigma A_S(\varepsilon_S T_S^4 - \varepsilon_{env} T_{env}^4).\end{aligned} \tag{45}$$

(T_S the temperature of the substrate surface, T_H the temperature of the substrate holder, T_{env} the temperature of the environment of the substrate (plasma, wall), α the accomodation coefficient, χ the molecular heat conductivity of the gas, p the gas pressure, λ_S the heat conductivity of substrate and holder, ε_S the emissivity of the substrate, σ the Stefan–Boltzmann constant.)

Since plasma processing takes place at rather large range of gas pressures (10^{-2}–100 Pa), the pressure may have a pronounced influence on the loss by heat conduction of the plasma, see Fig. 11. At atmospheric pressure heat conduction by gases is independent on pressure. However, at low pressure the distance of the objects between which the energy is transported might be much smaller than the mean free path of the gas molecules. On

the other hand, by using a large sample holder on which the substrate is perfectly fixed (i.e. by He-backflow as cooling gas or conductive silver), the loss by convection of the gas is low compared to the conduction along the sample holder.

Radiation losses can also often be neglected. However, at very high temperatures (e.g. CVD) or when the heat contact between substrate support and surroundings is poor, the contribution of radiation must be taken into account.

Unfortunately, the material constants $(\alpha, \chi, \lambda_S, \varepsilon_S)$ can only be used under ideal conditions, which means ideal heat contacts, constant environmental temperature, homogeneous solids, and homogeneous heat fluxes. Because heat transfer coefficients and thermal conductivities in most real cases are unknown it is necessary to determine those quantities as well as the heat capacity $(C_S = m_S c_S)$ by calibration. This is possible by measuring and analyzing the time derivative of the temperature when the substrate temperature rises due to a known thermal power at the substrate [29].

Detailed information on the energy transfer can be obtained by time and space resolved measurements of the surface temperature T_S where the time steps between the measured temperature points need to be small compared to the characteristic macroscopic heating rates.

By neglecting the radiation and convection the thermal balance (Eqs. (43)–(45)) now results in

$$\dot{Q}_{in} = \varrho_S d_S A_S c_S \left(\frac{\mathrm{d}T_S}{\mathrm{d}t}\right) + \frac{\lambda_S}{d_S} A_S (T_S - T_H). \quad (46)$$

Solving the differential Eq. (46) yields

$$T_S(t) = T_H + \dot{Q}_{in} \frac{d_S}{\lambda_S A_S} \left(1 - \exp\left(\frac{-\lambda_S}{d_S^2 \varrho_S c_S} t\right)\right), \quad (47)$$

which provides the possibility for a determination of the heat flux $\dot{Q}_{in}$ from the change of the temperature with time.

Initially, during surface treatment by a plasma, the energy influx will exceed the heat output and T_S will rapidly rise until a stationary state is reached. Fig. 15 shows two examples of temperature curves measured by a thermocouple glued on the substrate surface at a-C:H deposition in a supersonic cascaded arc plasma reactor [66]. At the beginning of the plasma–substrate interaction ($t = 0$, $T_S = T_H$) the heat losses can be neglected. The relation between the initial slope $(\mathrm{d}T_S/\mathrm{d}t)_{t=0}$ and the total power inflow $\dot{Q}_{in}$ can be determined from the time derivative of T_S:

$$\dot{Q}_{in} = \dot{Q}_S = C_S \left(\frac{\mathrm{d}T_S}{\mathrm{d}t}\right)_{t=0}, \quad (48)$$

where $C_S = m_S c_S = \varrho_S d_S A_S c_S$ is the heat capacity of the substrate which is used as a kind of calorimeter probe.

After some time $(t \to \infty)$ the temperature of the substrate becomes stationary (T_S^∞). At this point the heat flux from the plasma to the substrate $(\dot{Q}_{in})$ equals the heat flux from loss processes $(\dot{Q}_{out})$ and because $(\mathrm{d}T_S/\mathrm{d}t)_{t=\infty} = 0$ one obtains for T_S^∞:

$$T_S^\infty = T_H + \dot{Q}_{in} \frac{d_S}{\lambda_S A_S} = const. \quad (49)$$

When the plasma (heat source) is switched off, at time $t = t_{off}$, the influx is zero $(\dot{Q}_{in} = 0)$ and the temperature decreases according to

$$T_S(t) = T_H + (T_S^\infty - T_H) \exp\left(-\frac{\lambda_S}{d_S^2 \varrho_S c_S}(t - t_{off})\right), \quad (50)$$

see also Fig. 16. If the combinations of the material constants are known or determined experimentally the integral power influx $\dot{Q}_{in}$ can be obtained by a best fit of the measured $T_S(t)$ curve [83].

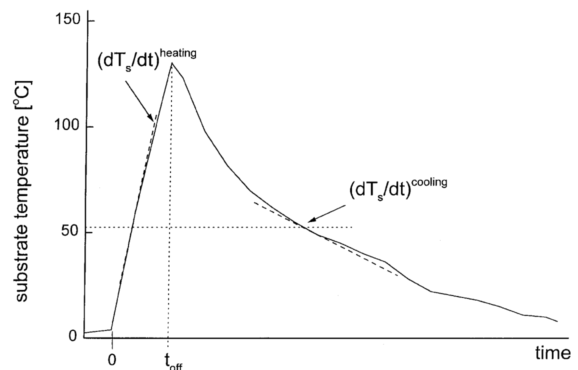

Fig. 16. Schematic plot of typical evolution of substrate temperature obtained during planar magnetron experiments by Thornton [84].

A quite similar procedure for the determination of the total heat influx has been used by Thornton [16,84] and Wendt et al. [29]. The heat flux measurements were made by observing the rate of temperature rise of a wafer which was spot-welded to a thermocouple and placed within a solid shield of much larger mass. The wafer was only fixed by the thermocouple and no other contact of the wafer to the shield and holder was realized. Hence, the conduction heat losses could be neglected.

$$\dot{Q}_{in} = C_S\left(\frac{dT_S}{dt}\right) + 2\varepsilon_S\sigma A_S(T_S^4 - T_{env}^4). \quad (51)$$

The radiation losses were estimated by measuring the slope of the cooling curve $(dT_S/dt)^{cooling}$ at the same temperature at which the heating slope $(dT_S/dt)^{heating}$ was measured, see Fig. 16.

During the heating phase the slope is

$$\left(\frac{dT_S}{dt}\right)^{heating} = \frac{\dot{Q}_{in}}{C_S} - \frac{2\varepsilon_S\sigma A_S(T_S^4 - T_{env}^4)}{C_S} \quad (52)$$

and because of $\dot{Q}_{in} = 0$ for the cooling phase one obtains

$$\left(\frac{dT_S}{dt}\right)^{cooling} = -\frac{2\varepsilon_S\sigma A_S(T_S^4 - T_{env}^4)}{C_S}. \quad (53)$$

If the slopes are determined at the same temperature T_S and assuming no change of the environmental temperature T_{env} due to the large heat capacity of the shield the difference of Eqs. (52) and (53)

$$\frac{\dot{Q}_{in}}{C_S} = \left(\left(\frac{dT_S}{dt}\right)^{heating} - \left(\frac{dT_S}{dt}\right)^{cooling}\right)_{T_S} \quad (54)$$

is a quantity proportional to the thermal power at the substrate [51,85].

In comparison to the described temperature rise methods there is another simple and reliable procedure to measure the heat influx at the substrate by determination of the temperature gradient along the sample holder [20]. Here the power flux is measured in steady state according to Eq. (49) which gives

$$\frac{\dot{Q}_{in}}{\lambda_S A_S} = \frac{T_S^{\infty} - T_H}{d_S} \approx \frac{\Delta T}{\Delta x}. \quad (55)$$

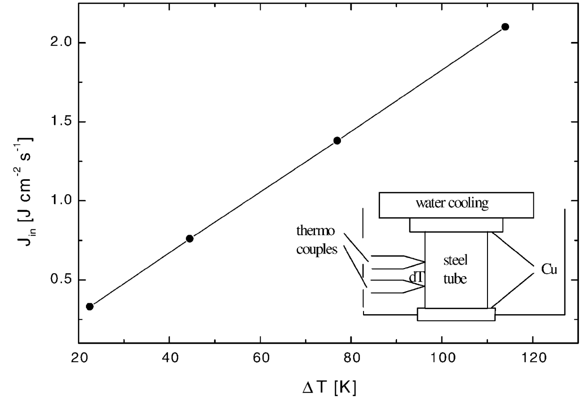

Fig. 17. Calibration: integral energy influx vs. measured temperature difference between two thermocouples, from [20].

By using a tube between substrate and water cooling the heat capacity and effective heat conductivity can be lowered (see Fig. 17). The calibration of the differential expression $\Delta T/\Delta x$ can be done by means of an electrical heater of known power. Thus, by using such a calibration the integral influx can be determined from the measured temperature gradient along the substrate holder tube.

A similar measurement combined with the pyrometer method has been performed by Tandian et al. [42]. They determined the heat transfer in an RF plasma torch for sintering. The energy balance measurements were primarily based on a calorimetric technique which employs the determination of the surface temperature of the sample and the several temperatures of the plasma (at inlet and exhaust) as well as of the cooling water at different locations.

It should be emphasized again that the measured energy influx $\dot{Q}_{in}$ is an integral value containing the several energy contributions which have been discussed in more detail in Section 2.1. In principle, a determination of the different energetic contributions as radiation, kinetic energy of striking particles, reaction enthalpy, etc. is possible by an analytical description. But in most cases of technological application the necessary data are not available. Therefore, fitting procedures have to be employed. In order to study the complex energy transfer mechanisms in low-pressure plasmas one should study at first rather

simple processes like thermal evaporation or ion beam assisted deposition (IBAD), where only one or two contributions dominate the energy influx to the substrate.

In most applications one can assume an uniform energy influx because the volume of the plasma is large compared to that of the treated substrates. However, in some cases the spatial profile of the substrate surface temperature must be taken into consideration which can cause non-uniformities in layer growth and morphology. For an example, Oakes et al. [86] measured a radial temperature profile under typical growth conditions using a thermal imaging camera (Fig. 18).

A radial temperature profile along the substrate can be caused by radial inhomogenities of the heat flux [87] or by an inhomogeneous heat transfer inside the substrate. Such a radially inhomogeneous heat flux in the plasma may be described by a Gaussian profile

$$\dot{Q}_{in} = \dot{Q}_{in0} \exp(-r^2/R^2_{\dot{Q}_{in}}), \tag{56}$$

where $\dot{Q}_{in0}$ is the heat influx at the axis, r the radial coordinate and $R_{\dot{Q}_{in}}$ is the half-width at half-maximum. In such cases of non-uniformities it is necessary to measure the surface temperature at different positions on the substrate.

3.2. Surface temperature measurements

For the experimental determination of the surface temperature T_S a broad variety of methods exists. As already mentioned above, for many applications the use of contact thermocouples is sufficient. In these cases the thermocouples, which must be chosen for the relevant temperature range, have to be connected to the substrate very carefully because the plasma environment has not the same temperature as the substrate, and the heat conductivity of a low-pressure plasma is very poor. The solid contact can be realized by conductive silver or by spot-welding. Anyway, the use of thermocouples for temperature measurements in a low-pressure plasma environment requires a careful analysis of the obtained temperatures as proposed, for example, by Piejak et al. [26].

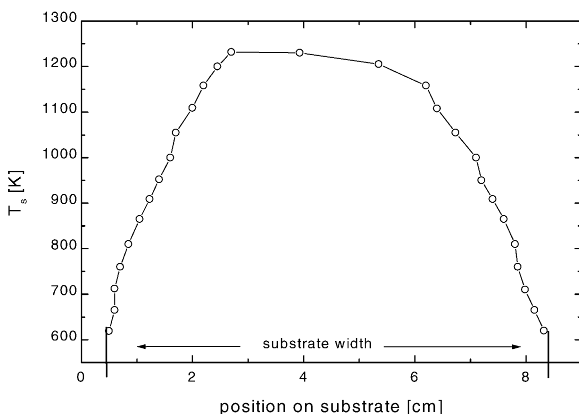

Fig. 18. Substrate temperature profile along a substrate during diamond growth with an oxygen–acetylene flame, from [86].

In applications, where thermocouples and other metallic connections to the surface should be avoided, determination of the resistivity may be favored. This method, which is based on the temperature dependence of the electrical resistance during heating, is often used for investigations that require ultra-high purity of the crystal and its surface [88].

Unfortunately, contact thermocouples or thin film resistors may affect the real substrate temperature or the indicated temperature by heat loss through the leads. If this disturbance shall be avoided, non-contact thermocouples are applicable to monitoring substrate and shield temperatures during plasma processing [89]. However, the use of this method requires the development of a model in order to understand the sensor behavior based on the heat transport in the region of the sensor. Such a detailed description of the heat exchanges have been studied by an interesting electrical model proposed in [23].

A non-contact method to measure the surface temperature is by means of pyrometers using the infrared radiation emitted by the substrate [42]. However, this method is only reliable if there is no change in the emissivity of the surface during the plasma process. For instance, in thin film deposition experiments the emissivity of the substrate surface changes by film growth. A very sensitive and suitable surface temperature measurement can be realized by fluoroptic methods [2,72]. Fluoroptic thermometry is a convenient way to execute in-situ measurements in RF plasmas, since such measurements are not disturbed by the electrical discharge and the reactive environment [43].

Other procedures of non-contact measurements of the surface temperature use the change in mechanical and optical properties of solids by temperature variation. Changes in substrate temperature induce thermal expansion of the substrate. A diffracting grating etched onto the sample surface expands itself according to the temperature and the observation of the diffraction pattern can be employed for determining T_S [67,90]. In another way the thermal expansion of sandwich substrates with different refractive indexes can be observed by ellipsometry [91] or by near infrared (NIR) interferometry using a double-sided polished wafer [92].

Interferometric techniques for temperature measurements hold much promise for noncontact thermometry of semiconductors, since the temperature coefficient of refraction is almost two orders of magnitude greater than the thermal expansion coefficient. When a semiconductor wafer is heated, the change of its optical thickness corresponds to many times the wavelength of visible light. As a consequence, it is possible to register numerous interference maxima and minima which can be used for calculation of temporal variation in wafer temperature [93,94]. For example, Magunov [95] used the temperature dependence of the optical thickness of silicon acting as a Fabry–Perot interferometer at the radiation of an infrared He–Ne laser ($\lambda = 1.15\,\mu m$) for monitoring plasma etching of polymers in an oxygen discharge. A review of new fast-developing techniques based on measurements of temperature-sensitive optical parameters in comparison to conventional methods (thermocouples, radiation) may be found in [96].

Finally, we mention a fast and extremely sensitive method for reversible thermal analysis of very small solid samples which uses a micromechanical calorimeter based on the deflection of a bimetallic cantilever [97].

4. Results: examples for energy balances during plasma processing

Low-temperature plasma processing of solid surfaces is essentially affected by energetic and thermal quantities, as energy per incoming particle (E_v), particle flux (j_v), energy flux density (energy dose, $J_v = j_v E_v$) from the plasma and electrodes, and substrate temperature (T_S).

If the substrate is additionally heated by an external source (substrate heater), it is difficult to distinguish between the different contributions to the heating process. Only in suitably chosen experimental devices the effect of a single quantity as listed above can be separately investigated.

In the following sections we will illustrate the influence of the different energetic and thermal quantities at some examples of thin film deposition, plasma etching, and surface modification.

4.1. Thin film deposition

The importance of ion energy and ion flux at low-temperature silicon epitaxy using a low-energy ion bombardment process has been reported, for example, by Shindo et al. in [98]. In their study the effects of ion bombardment and the related energy dose on the crystallinity of the grown silicon film has been investigated in detail. An RF-DC-coupled mode bias sputtering system has been used for silicon growth. A 100 MHz RF power supply was employed to generate a high density plasma at a gas pressure of 1.33 Pa. Furthermore, two DC power supplies were connected to the target and to the substrate holder, respectively, via low pass filters. By this method, the DC potentials could be separately controlled. The ion bombardment energy was determined by the potential difference between the time-averaged plasma potential and the externally applied substrate DC voltage. On the other hand, the RF power input controls the plasma density, i.e. the ion flux provided to the substrate surface. Thus, by adjusting the target bias, the substrate bias, and the RF power the essential parameters in deposition such as growth rate and ion energy flux have been selected to fit any desired conditions. In the experiments the principal deposition variables investigated were ion flux and ion bombardment energy as well as substrate temperature measured by thermocouples during Si film growth, while maintaining constant the deposition rate at about $10\,nm\,min^{-1}$.

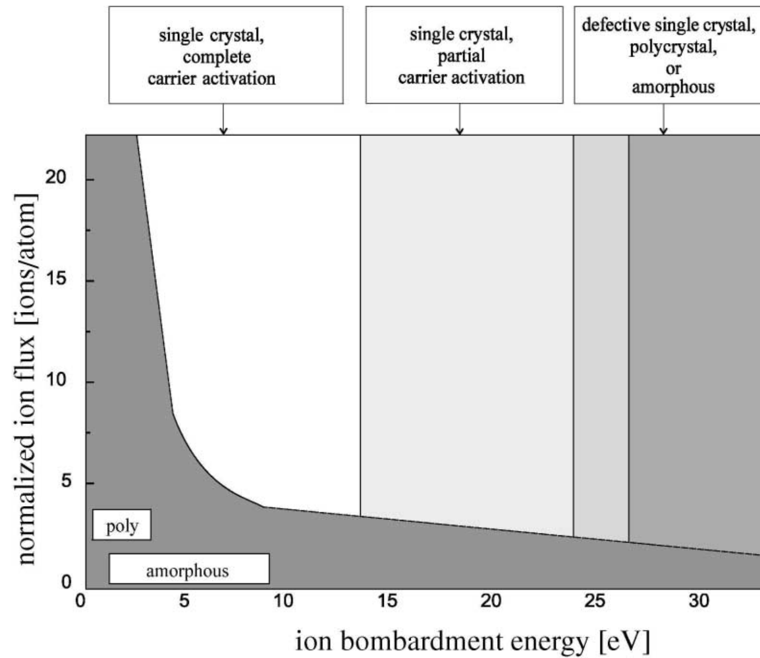

Fig. 19. The dependence of silicon film crystal structure on ion kinetic energy and normalized ion flux, from [98].

Very similar to former studies of Thornton [99], Shindo et al. found characteristic regions in the $E_{i,kin} - j_i$-plane of different crystal structures, see Fig. 19 [98]. Only in the characterized region of Fig. 19, characterized by low kinetic ion energy and high normalized ion flux, single crystal films with fully activated carriers were obtained due to the low deposition temperature. Furthermore, it could be demonstrated that at low-temperature bombardment with heavy ions (Xe^+) was more effective in promoting epitaxy than Ar^+ ion bombardment.

On the other hand, the resistivity of the deposited silicon films were affected by the ion energy influx and the resulting substrate temperature, too. In Fig. 20, the resistivity of silicon films grown at different temperatures as function of the ion kinetic energy at constant ion flux density is shown. It is interesting to note that low-resistivity films for the temperature investigated were only formed when the ion energy was higher than 7 eV. At energies higher than 15 eV the film resistivity increases for all flux densities due to the dotand deactivation. Otherwise, for an increasing ratio of argon ions to incoming silicon atoms, low-resistivity films are realized even at lower ion kinetic energies of about 3 eV.

Unfortunately, it is not always possible to study separately the influence of kinetic ion energy, because in typical process plasmas the involved energetic parameters act together. Therefore, ion beam processes are favored for the investigation of the role of ion energy. This method, for example, has been used in the production of dense diamond-like sp^3-bonded phase carbon films by means of a C^+-ion beam by Grossmann et al. [101]. Summarizing, they obtained the following results for the carbon film properties during ion beam deposition:

- carbon films with significant amounts of sp^3-bonding larger than 40% could be deposited at room temperature over a wide energy range (30 eV–10 keV) of the C^+-ions (Fig. 21a),
- the suppression of the sp^3-bonding at $E_{i,kin} \leqslant 20$ eV or $E_{i,kin} \geqslant 10$ keV is associated with an increase in film roughness (Fig. 21b),
- high fractions of sp^3-bonding are associated with subsurface growth of atomically smooth layers,

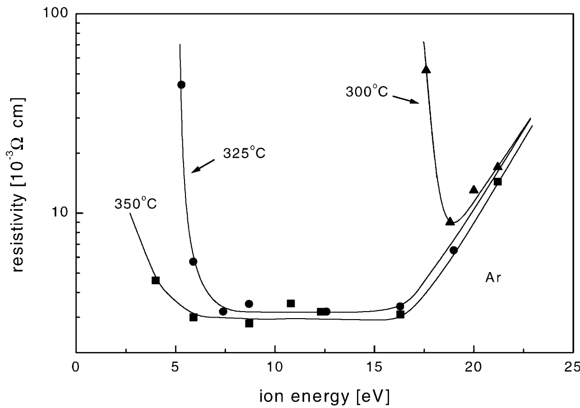

Fig. 20. The resistivity of silicon films grown at different T_S as a function of ion kinetic energy, from [98].

- the suppression of sp^3-bonding of very high energetic C^+-ions is due to ballistic effects of high-energy implantation and the resulting enhanced bulk diffusion.

The role of ions and their transfered momentum and deposited power is a key parameter in the formation of cubic boron nitride films, too, as reported for instance by Mirkarimi and coworkers [100]. The authors varied the ion energy in conjunction with the ratio of ion flux to depositing atom flux. In their series of systematic measurements they found a window of the ratio in which large c-BN percentages are obtained. There is a critical value of this ratio above which c-BN formation is initiated and a point at which the ratio is too large. In this region the films begin to be completely sputtered away.

In the following parts, the influence of substrate temperature and energy flux on film deposition will be discussed for some further examples obtained by own experiments.

4.1.1. Temperature dependence of glow discharge polymerization and carbon film growth

As shown in the examples given above, the ion energy influx during silicon and carbon deposition influences characteristic film properties as crystallinity, binding states and resistivity. However, not only the film properties but also the growth rate itself is influenced by the energy influx and the resulting thermal conditions.

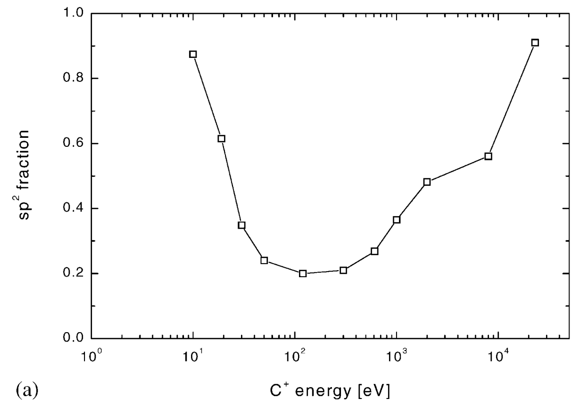

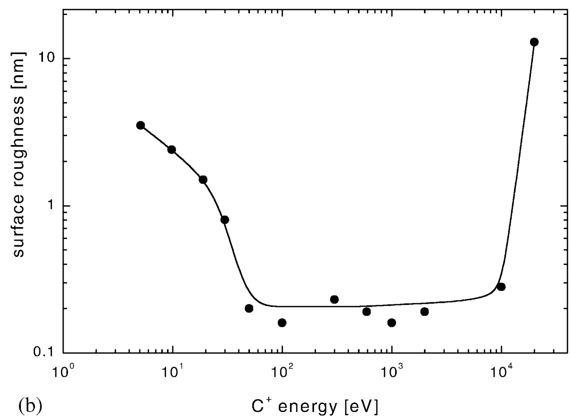

Fig. 21. (a) sp^2-fractions and (b) surface roughness of 100 nm carbon films on room temperature silicon substrates in dependence on C^+-ion energy [101].

The following example of plasma polymerization will illustrate the influence of thermal conditions at the substrate upon surface reactions and therefore upon the deposition rate of polymer films. In [102] an extensive system of equations has been proposed to determine the growth rate of thin polymer layers induced by gas discharges. The description includes activation reactions and transport processes in the plasma volume as well as reactions at the surface. For the computation of the polymerization rate the authors distinguished between the two limiting cases [102]: flow-in model and adsorption model.

By means of the adsorption model the growth rate R_{pol} of the polymer film is given by

$$R_{pol} = \sum_{\mu} \sigma_{\mu} n_{\mu} j_x. \tag{57}$$

Here σ_μ is the reaction cross section for the incorporation of monomer molecules of kind μ into the thin film under the action of collisions with an energetic particle flux j_x (ions or electrons) and n_μ is the actual surface concentration of the monomer molecules. The quantity n_μ can be obtained from the balance equation

$$\frac{dn_\mu}{dt} = j_\mu \gamma_\mu \left(1 - \frac{n_\mu}{n_0}\right) - \frac{n_\mu}{\tau_{des,\mu}} - n_\mu \sigma_\mu j_x \tag{58}$$

(j_μ the monomer inflow, γ_μ the monomer sticking probability, $\tau_{des,\mu}$ the monomer residence time at the surface, and n_0 the substrate surface density), which yields in equilibrium state

$$n_\mu = \frac{n_0 \gamma_\mu j_\mu}{\gamma_\mu j_\mu + n_0(1/\tau_\mu + \sigma_\mu j_x)}. \tag{59}$$

The macroscopic measured polymer growth rate W is obtained as

$$W = \frac{M_\mu}{L\varrho_\mu} R_{pol}, \tag{60}$$

where M_μ denotes the molecular mass of the monomer, L is the Avogadro's number, and ϱ_μ the mass density of the film. The energetic ion flow $j_x = j_i/e_0$ can be obtained by measuring the ion current density j_i. The temperature dependence of the coverage n_μ/n_0 and, thus, also of the polymerization rate is essentially influenced by the residence time of the monomer molecules (Frenkel relation, see Eq. (33)) and the monomer particle flux j_μ. The monomer flux depends on the volume concentration N_μ and the gas temperature which is near the substrate surface identical with the surface temperature T_S:

$$j_\mu = \sqrt{\frac{k}{2\pi M_\mu}} N_\mu \sqrt{T_S}. \tag{61}$$

In the experiment referred here [4] polymer films have been deposited in the positive column ($r_0 = 1.75$ cm) of a benzene–neon glow discharge ($p_{Ne} = 133$ Pa, $p_{C_6H_6} = 6.7$ Pa, $I = 30$ mA). Externally heated cylindrical probes served as substrates. By variation of the probe temperature the T_S dependence of the growth rate which has been derived from the $I-V$ characteristic of the Langmuir probe covered by the polymer film could be obtained, see Fig. 22. The temporal change of floating potential V_{fl} of the probe has been employed for this purpose. The Ne^+-ions were found to be the dominant species in crosslinking the benzene monomers. The flux of Ne^+ has been measured to be about $j_x = j_{i+} = 2.5 \times 10^{16}\,\mathrm{cm^{-2}\,s^{-1}}$. The measured dependence of the polymer growth rate on the surface temperature (Fig. 22) has been described by a curve $W(T_S)$ calculated with the model given in Eqs. (57)–(61) with the following data: $\gamma_{C_6H_6} = 0.1$, $\tau_{des0} = 10^{-12}$ s, $E_{des} = 1.24$ eV, $\sigma = 2 \times 10^{-14}\,\mathrm{cm^2}$. The model shows that at relatively low temperatures the growth rate depends only on the monomer supply, while for $T_S > 700$ K the monomer coverage is the rate-limiting quantity for layer growth.

In addition to the adsorption model, the flow-in model (that means the direct incorporation of the ions into the film) has been taken into account by Keudell et al. in [103]. They measured the polymerization rate in a methane microwave discharge as a function on the substrate temperature by means of ellipsometry (Fig. 23).

For their modified model the authors used the following values: sticking coefficients for CH_3 radicals and for the ions were assumed to be unity. The residence time of the radicals has been calculated by the Frenkel relation with $E_{des} = 0.65$ eV and $\tau_{des0} = 10^{-12}$ s. The cross section for direct ion incorporation in the film was $7.7 \times 10^{-16}\,\mathrm{cm^2}$ and the cross section for the

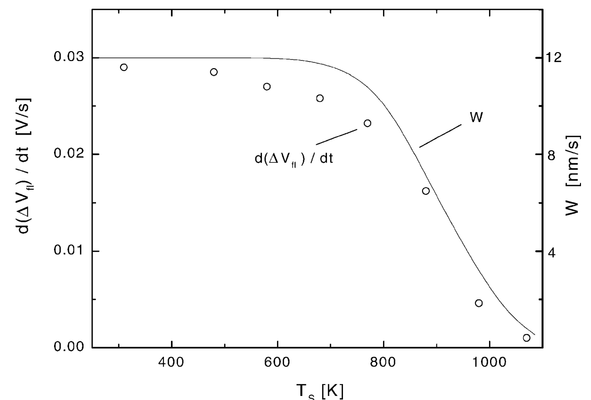

Fig. 22. Polymer growth rate in a C_6H_6–Ne glow discharge. (open circles: measurement, continuous line: model).

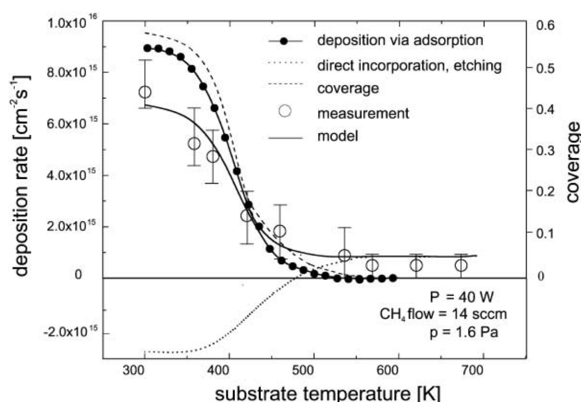

Fig. 23. Deposition rate vs. substrate temperature [103]. By solving the balance equations for the plasma densities (CH_3, H_2, H) the temperature dependence of the deposition rate can be determined.

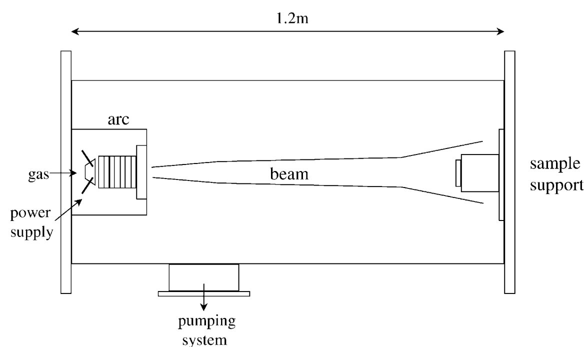

Fig. 24. Schematic of the cascaded arc reactor used for a C : H deposition.

hydrogen reactions with the physisorbed monomer particles was obtained as $6.8 \times 10^{-16}\,cm^2$, while the cross section for the hydrogen reactions with the deposited layer was $10^{-15}\,cm^2$. From the model two temperature regimes can be recognized: for substrate temperatures $T_S \leqslant 450\,K$ the polymerization via adsorption is dominated, whereas for temperatures $T_S \geqslant 450\,K$ direct incorporation of ions into the thin film is the dominant process determining the growth.

The deposition rate of amorphous, hydrogenated carbon films in dependence on the substrate temperature has been investigated in [66]. The experiments were performed in a reactor based on the supersonic expansion of a cascaded arc plasma in an argon/methane mixture (Fig. 24). In such a device a geometric separation has been realized for the three principal processes occurring in plasma deposition: plasma production (arc), plasma transport (beam), and plasma treatment (a-C : H deposition) are in separate sections of the apparatus. The experimental details are described more extensively in [104]. The film thickness was measured by using ellipsometry and the surface temperature was monitored by thermocouples.

The energy flux provided by the a-C : H deposition process heated the samples (glass or steel, respectively). Hence, in the course of plasma treatment, the combination of the measured film thickness versus time with the temperature versus time resulted in a relation between the deposition rate W and the surface temperature T_S. This relation is plotted in Fig. 25. The main contributions in substrate heating were the energetic argon atoms ($\approx 1\,eV$) in the supersonic plasma beam and the carbon film condensation. The negative slope of the temperature dependence $W = W(T_S)$ indicates again an adsorption–desorption equilibrium as rate limiting process in the temperature range studied. A relatively small variation of the temperature leads to a remarkable decrease of the growth rate.

From the measurements we obtained an activation energy for the desorption of the film forming species of $E_{des} = 0.58\,eV$ and a cross section of $\sigma = 3 \times 10^{-17}\,cm^2$ for the crosslinking of C atoms by the Ar bombardment. It can be concluded that the incorporation of the particles into a growing film may be intermediated by an adsorbed layer.

Not only the deposition rate of a-C : H films, but also their properties are influenced by the substrate temperature. This observation has been supported by Yoon et al. in studies of a-C : H film deposition by the ECR-CVD method [105]. In addition to the deposition rate the optical band gap and the intensity of C–H bondings in the IR spectra decreased significantly with increasing substrate temperature. The optical band gap variation with the supplied microwave power and, hence, with the energy influx from the plasma as well as with the substrate temperature was clearly correlated with the intensity of the C–H bonds and was related to the amount of bonded hydrogen in the layers.

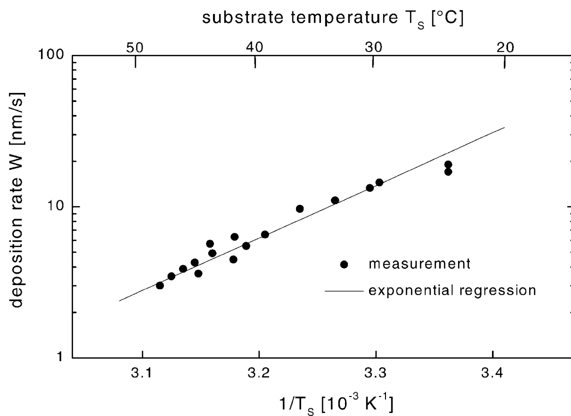

Fig. 25. Growth rate in dependence on the substrate temperature. The negative slope of the Arrhenius-plot indicates an adsorption–desorption equilibrium as rate limiting process.

A strong correlation between deposition temperature T_S and hydrogen content was observed in deposition of a-Si : H films in a supersonic reactor with a cascaded arc discharge, too [74].

4.1.2. Energy fluxes at Ti film deposition by hollow cathode arc evaporation and their effect on layer density

At titanium layer deposition with a hollow cathode arc discharge the integral energy influx to the substrate has been monitored by measuring the temperature gradients [20]. The total energy inflow $\dot{Q}_{in}$ during the deposition of titanium in a hollow cathode-arc evaporation device (HCAED) used in the experiments consists of the following portions: heat radiation from the molten material to the substrate, power transfered due to charge carriers, adsorption and condensation of vapor species. The loss processes $\dot{Q}_{out}$ are: heat radiation and heat conductivity from the substrate along the water-cooled sample holder (macroscopical cooling).

The characteristic feature of a HCAED is the hollow cathode arc with a rather high ionization degree which has three functions: activation of the particles near the substrate, activation and cleaning of the substrate surface and transformation of solid titanium into the vapor phase. The experimental set-up (see Fig. 26) and the principle of the hollow cathode arc have been described elsewhere [20,106].

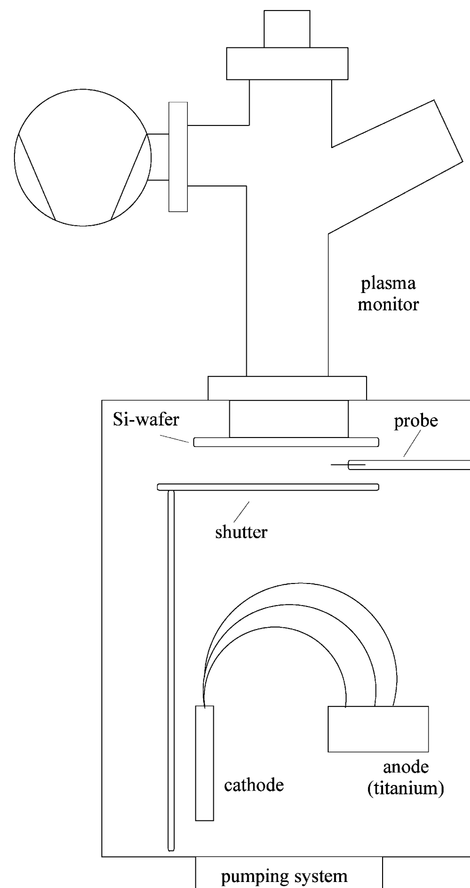

Fig. 26. Experimental set-up of the HCAED for titanium deposition, schematic.

The experimental standard conditions were as follows: arc current 130–240 A, arc voltage 20–27 V, discharge power 2.5–6.4 kW, substrate voltage -80–0 V, gas pressure 0.2 Pa, Ar gas flow 95 Pa l s^{-1}, deposition rate of titanium 0.1–2 nm s^{-1}, distance anode–substrate 18 cm, and surface temperature 40–200°C. In order to vary the energy influx towards the substrate discharge power and bias voltage of the substrate have been changed. The integral energy flux density to the substrate was determined by means of a measuring head which has been already shown in Fig. 17.

Simultaneously to the determination of the energy flux the electrical current (I_S) towards the substrate and the plasma parameters (n_e, kT_e, V_{pl}) in front of the substrate were determined by means of a Langmuir probe. The energy distribution and the ratio between the argon and titanium ions in dependence on the discharge power were measured by energy-resolved mass spectrometry (plasma monitoring). Film thicknesses and deposition rates have been obtained by means of ellipsometry during the titanium deposition on silicon wafers. For the estimation of the layer density Rutherford backscattering (RBS) was employed.

The contribution J_c due to condensation of titanium vapor to the integral energy flux density has been estimated according to Eq. (20). By using the relevant values for the Ti film density ($\varrho = 3.5-3.9\,\mathrm{g\,cm^{-3}}$) and the deposition rate as given above the contribution of J_c is in the order of $0.05\,\mathrm{J\,cm^{-2}s^{-1}}$. This contribution is negligibly low compared to the radiation and the part of charge carriers in HCAED titanium deposition.

As introduced in Section 2.1.2, the energy-flux densities of the charge carriers are given by the product of the particle flow densities to the substrate and the mean particle energies. For a Maxwellian energy distribution, as it was valid under our experimental conditions, the flux densities of the charge carriers to the substrate, which was negatively biased in respect to the plasma, have been determined according to Eq. (14) [107] for the ions and Eq. (17) for the electrons. The measured values of the electron density n_e was in the order of 5×10^{16}–$3\times10^{17}\,\mathrm{m^{-3}}$ depending on the discharge power and the mean electron energy kT_e was about 5 eV. The transfered kinetic energy of the electrons was obtained by Eq. (16) and the kinetic energy of the ions by Eq. (9).

The contributions of the charge carriers to substrate heating depend strongly on the bias voltage which consists of the external substrate voltage V_S and the plasma potential V_{pl}, while the contribution of the radiation J_{rad} of the molten titanium depends only on the discharge power and is not influenced by the bias voltage. Therefore, this contribution could be separated by a variation of V_S (Figs. 27 and 28). For $V_S \leqslant -30\,\mathrm{V}$ the

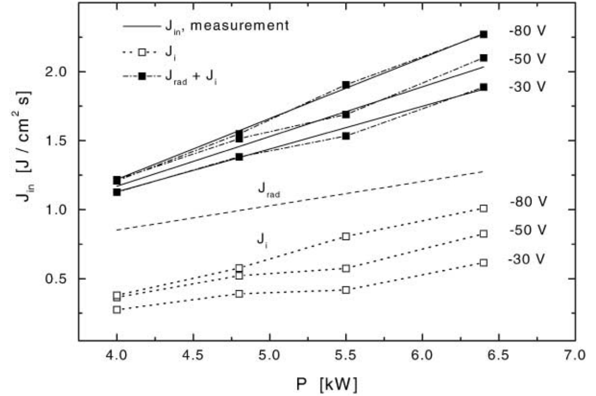

Fig. 27. Integral energy inflow at Ti deposition in HCAED for $V_S \leqslant -30\,\mathrm{V}$.

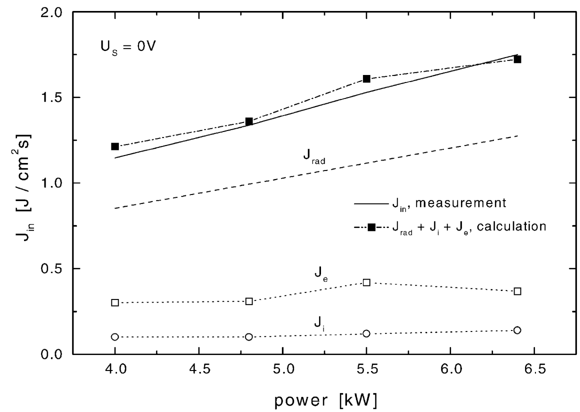

Fig. 28. Integral energy inflow at Ti deposition in HCAED for $V_S = 0\,\mathrm{V}$.

electron flux density to the substrate is $j_e \simeq 0$. Under these conditions only the energy flux due to the ions and radiation have to be taken into account. In this case, the part of radiation J_{rad} can be determined from the difference between the measured total energy inflow (J_{in}) and the calculated contribution of ions J_{i+}:

$$J_{rad} = J_{in} - J_{i+}. \tag{62}$$

This calculation was done for three substrate voltages: -30, -50, $-80\,\mathrm{V}$. The mean value is shown as J_{rad} in Figs. 27 and 28. These calculated values are compared with the measured total energy inflow (drawn lines in the upper part of Fig. 27). There is a good correspondence of the

calculations and measurements for the three different substrate voltages. The electrons have to be considered in the case of $V_S \rightarrow 0$. As an example for the electron influence the results for $V_S = 0\,\mathrm{V}$ are shown in Fig. 28, where the calculated parts of the ions, electrons and radiation, respectively, are presented. The sum of these three contributions is compared again with the measured integral inflow which is marked by the drawn line.

For all considered substrate voltages the heat radiation is the dominating part for substrate heating in hollow cathode arc evaporation of titanium, followed by the part of the charge carriers. For $V_S \leqslant -30\,\mathrm{V}$ only the ions determine the contribution of the charge carrier, while for $V_S \rightarrow 0$ the part of the electrons becomes more important.

But the importance of the charge carriers in regard to layer deposition is not only for substrate heating. Moreover, the ions are often the essential component to improve the film quality by ion mixing, etc. A relatively small portion of ions may change the properties of a deposited layer in a drastic manner. For instance, an ion irradiation of the growing film influences the acceleration of the nucleation stage, destruction of columnar structure, modification of crystal orientation, and stoichiometric changes. As it will be shown, in our case especially the layer density has been influenced by the ions.

The plasma of the HCAED contains Ar ions as well as Ti ions which both have an energetic influence to the substrate surface. Therefore, the ratio between the ionic species in dependence on the discharge power was of special interest.

Combining the total ion saturation current I_S determined by probe measurements and the relation between the contributions of the several ion species measured with energy resolved mass spectrometry, the flux of Ar^+, Ar^{2+}, Ti^+ and Ti^{2+} to the substrate could be estimated [21]. The slope of the several ionic portions as functions of discharge power is presented in Fig. 29. It is obvious that at low power the argon ions are the dominating species whereas at higher discharge power ($\geqslant 4.5\,\mathrm{kW}$) titanium ions become important. At high power there is a large supply of titanium vapor and because of the greater ionization cross section of titanium compared with argon the metal vapor can be ionized more effective than the inert gas [108]. The degree of ionization for titanium may reach values up to 20%.

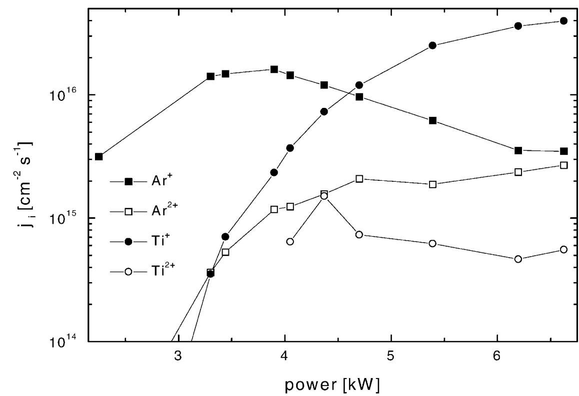

Fig. 29. Ion flux densities j_i in dependence on discharge power.

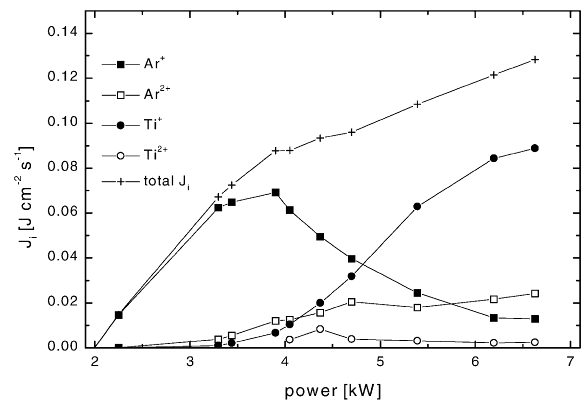

Fig. 30. Energy inflow J_i by the various ion species.

Finally, the total energy flux by the ions as indicated in Fig. 28 could be separated into different energy fluxes supplied by the various ion species. The result is plotted in Fig. 30.

The variation in the ion composition with discharge power can also be seen in a remarkable change in the density of the deposited titanium films. In the power range dominated by the Ti ions the mass density is essentially higher [109]. Not the whole energy of the ions seems to be decisive for the layer density. Only the part of the Ti ions is of

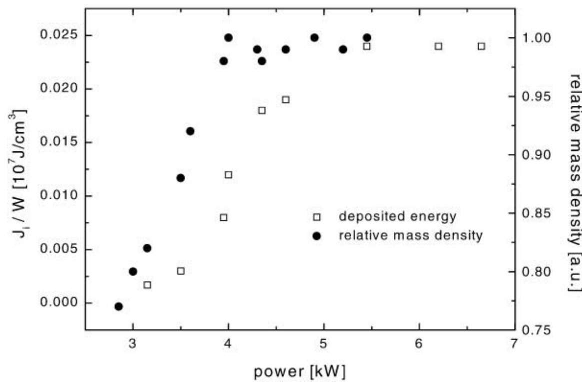

Fig. 31. Relation between energy inflow supplied by titanium ions and film density.

importance. The energy flux density of the Ti-ions (Ti^+, Ti^{2+}) divided by the deposition rate in dependence on discharge power shows a very similar behavior as the mass density of the deposited layer (Fig. 31). In a similar manner the relationship of the ion concentration to the neutrals have also been found by other authors to be as an indication for the mass density of the deposited material [13].

4.1.3. Influence of energetic contributions during DC-magnetron sputtering of aluminum films on microstructure

A characteristic feature of thin film deposition by magnetron sputtering in comparison to thermal evaporation is the higher kinetic energy of the particles arriving at the substrate. The integral energy influx ($\dot{Q}_{in}$) during sputtering influences the thermal conditions at the substrate surface and, hence, in addition to momentum transfer it affects the microstructure and morphology as well as adhesion and residual stress of the deposited films [1,13].

In the following example of aluminum sputtering (Fig. 32), the measured total energy influx, which has been determined from the rise of the substrate temperature (dT_S/dt) during the sputtering process, consists mainly of the kinetic energy of charge carriers and sputtered particles, and the released condensation heat [55].

The contribution of ions (J_i) and electrons (J_e) could be distinguished again by variation of the substrate potential. The effect of sputtered particles on the energy balance ($J_{n,sput}$) is estimated by the product of their flux density and the mean kinetic energy which has been determined from the energy distribution of sputtered species. Finally, the contribution J_c due to condensation of aluminum particles has been determined by measuring the deposition rate and by taking into account the specific condensation heat.

The Al films were sputtered by a DC magnetron onto glass or silicon substrates, respectively, or onto microdisperse powder particles. In Fig. 32, the experimental set-up for the Al deposition is presented. The discharge voltage was operated at 250–550 V and the current range was 20–250 mA. Standard argon gas pressure was 0.01 mbar at a gas flow rate of 50 sccm. The distance between target and substrate could be varied between 4 and 15 cm. Opposite to the magnetron, at the bottom of the reactor an RF electrode was installed, which was necessary for charging and trapping of injected powder particles in order to modify them [110].

The discharge has been studied by several diagnostics. Langmuir-probe measurements and self-excited electron resonance spectroscopy (SEERS) [111] provided information on the electrons whereas the ion and neutral component was monitored by energy resolved mass spectrometry. The deposited films were investigated by analytical techniques as scanning electron microscopy (SEM), X-ray-photoelectron spectroscopy (XPS), Rutherford-backscattering (RBS), and atomic force microscopy (AFM).

In the present study the internal plasma parameters as V_{pl}, V_{fl}, n_e, kT_e, etc. have been measured in the substrate region which is relevant for the fluxes to the substrate. The measurements of the plasma parameters have been carried out for only the RF discharge as well as for the combined operation of RF plasma and DC magnetron as it was commonly used in powder treatment. Of course, in magnetron operation the plasma parameters in comparison to the weak RF discharge are remarkably changed. For example, comparing the spatial distributions of the floating potential in Fig. 33, one can recognize two essential differences. At first, the floating potential in case of

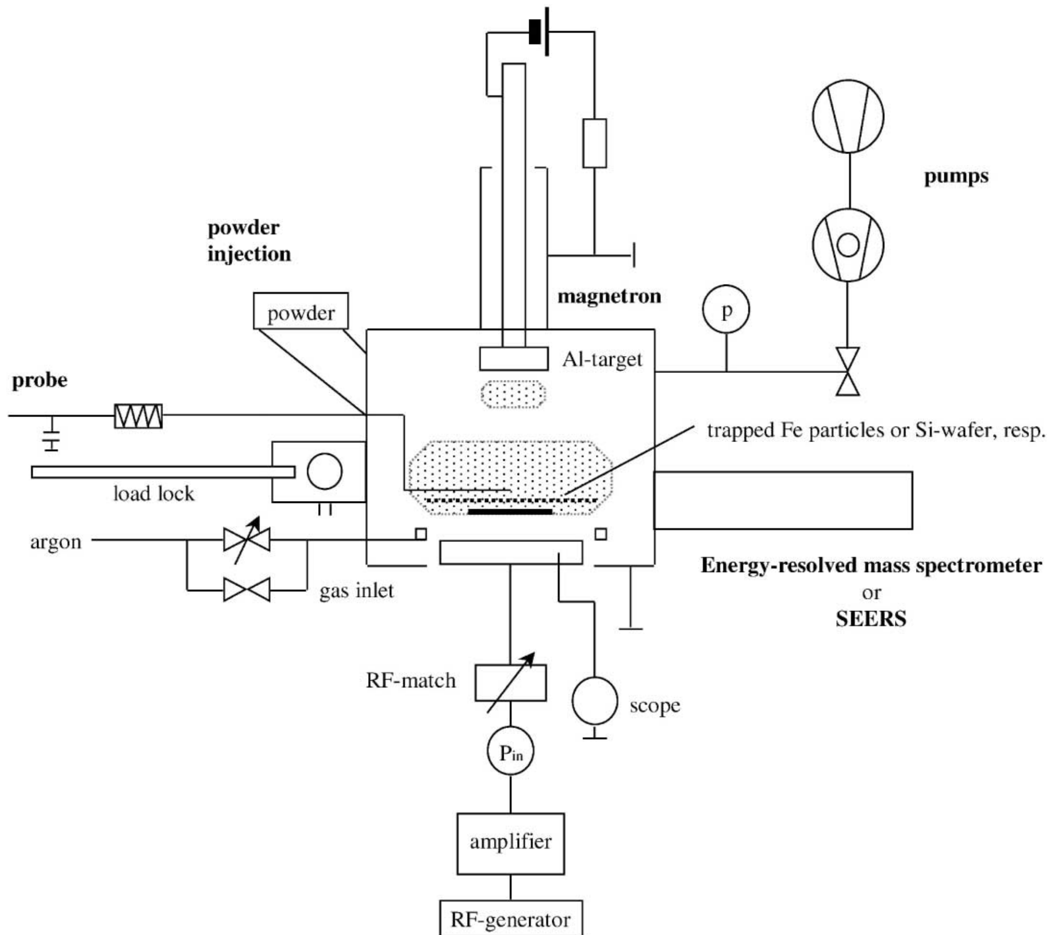

Fig. 32. A schematic view of the experimental set-up for aluminum sputtering onto flat substrates and powder particles.

magnetron operation is much more negative as for the RF plasma and, secondly, the spatial distribution is now more flat. The ion energy distribution (IED) reflects the remarkable differences between both discharge regimes [55].

From the number of ions arriving at the target and their mean energy the yield and, hence, the flux of sputtered Al particles (j_{Al}) to the substrate has been estimated using TRIM to be in the order of a few $10^{16}\,\mathrm{cm}^{-2}\,\mathrm{s}^{-1}$ for our experimental conditions (Fig. 34b). Supposing that all sputtered Al atoms which strike the substrate also stick on it, one can simply calculate the growth rate. The calculated Al deposition rate R_{dep} is in quite good accordance with the rates measured by RBS and optical transmission, respectively, as it can be seen in Fig. 34c.

The energy influx to the substrate and, consequently, the substrate heating during sputter deposition with a magnetron source is a combination of different heating contributions. As is the case for all vapor deposition processes, the heat of condensation (J_c) must be considered, which is for aluminum in the order of $q_c = 10^4\,\mathrm{kJ\,kg}^{-1}$ ($E_c = 3.3\,\mathrm{eV\,atom}^{-1}$). The contribution J_c to the energy influx due to film condensation is corresponding to Eq. (20):

$$J_c = q_c \varrho W_{dep} = j_{Al} E_c. \tag{63}$$

(W_{dep} the deposition rate, ϱ the mass density.)

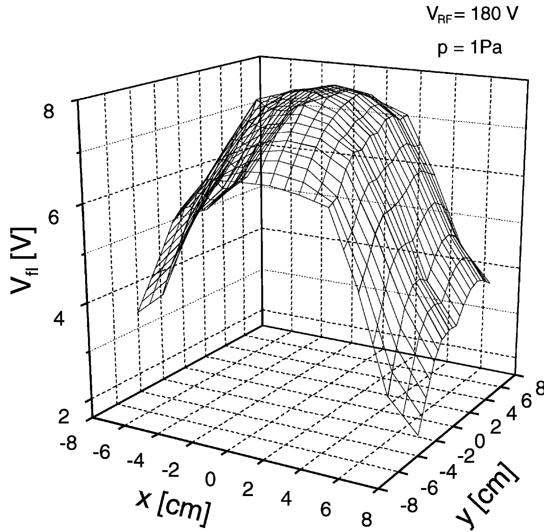

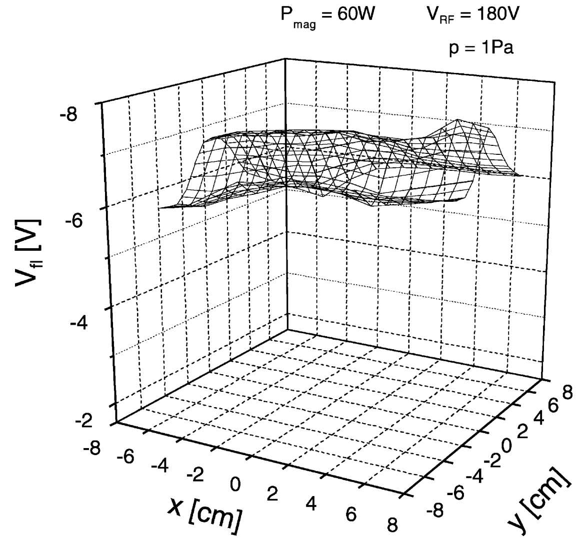

Fig. 33. Spatial variation of the floating potential at $z = 5\,\text{cm}$ above the RF electrode. The RF electrode is in the $x{-}y$ plane.

The contribution J_{ch} due to the kinetic energy of charge carriers (electrons and Ar ions) depends on the electron density in the substrate region and the mean kinetic energy of the carriers which is determined by the bias potential $V_{bias} = V_{pl} - V_S$. Because the substrates were always at floating potential, it is $V_S = V_{fl}$. The energetic contributions (J_e, J_{i+}) of the charge carriers have been obtained according to Eqs. (16) and (17) and Eqs. (9) and (14):

$$J_e = n_e\sqrt{\frac{kT_e}{2\pi m_e}}\,\mathrm{e}^{-eV_{bias}/kT_e}2kT_e,$$

$$J_{i+} = n_e\sqrt{\frac{kT_e}{m_i}}\,\mathrm{e}^{-1/2}\mathrm{e}_0 V_{bias}. \tag{64}$$

The electron energy was $kT_e = 4.2\,\text{eV}$ and the electron density in the substrate region during sputtering was measured to be in the order of $n_e = 5\times10^8$–$3\times10^9\,\text{cm}^{-3}$ depending on the discharge power (Fig. 34a). The first equation in (64) represents the energy influx by electrons in case of a Maxwellian energy distribution. However, if the EEDF is of another type, the contribution of the electrons might differ as illustrated in Fig. 7.

In case of floating substrates the released recombination energy flux J_{rec} has to be considered

$$J_{rec} = j_{i+}E_{rec}, \tag{65}$$

where $j_{i+} = j_e$ and E_{rec} is the ionization energy, which is for argon 15.7 eV.

Due to low operating pressure of the magnetron, a significant fraction of the kinetic energy E_n of the sputtered Al atoms may still be present for the depositing atoms in the substrate region. This contribution $J_{n,sput}$ is then

$$J_{n,sput} = j_{Al}E_n = W_{dep}\frac{N_A\varrho}{M}E_n. \tag{66}$$

The kinetic energy E_n of the sputtered neutrals has been calculated by TRIM [64] for a magnetron discharge voltage of 440 V, see Fig. 35a. The simulation yields a mean value of $2.9\,\text{eV atom}^{-1}$. In addition, the energy distribution of the sputtered species has been experimentally obtained by plasma monitor measurements (Fig. 35b). In the measured spectra one can observe a peak due to the sputtered Al particles exactly at that position ($\approx 3\,\text{eV}$), which has also been obtained by TRIM simulation. If the target is covered by a shutter the

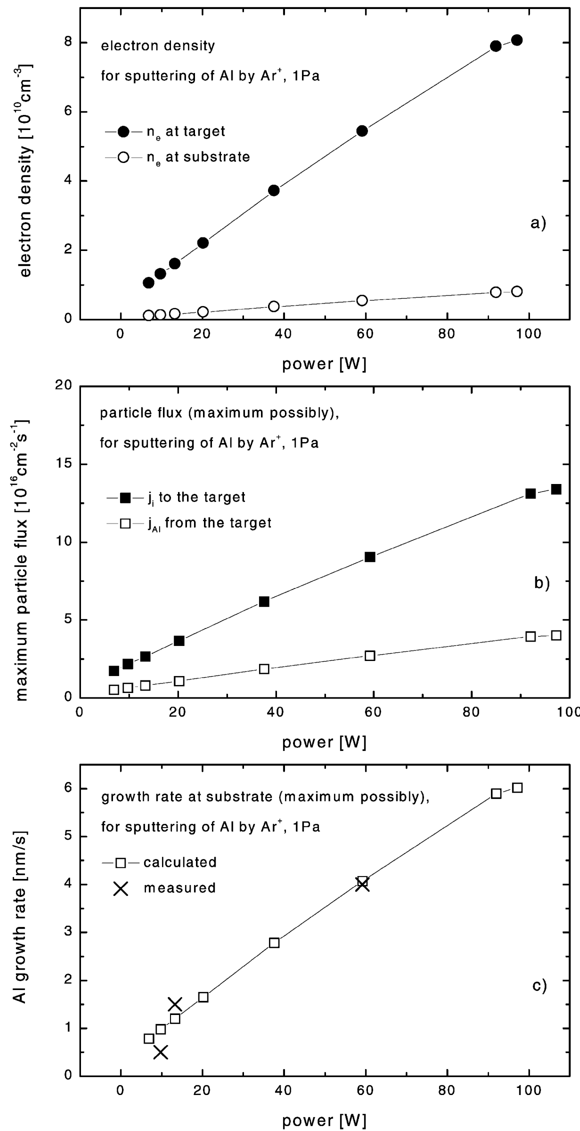

Fig. 34. Electron density (a), particle fluxes (b), and results of model calculation for Al growth compared with measured deposition rates vs. power (c).

Al atoms, which arrive at the substrate by diffusion, exhibit only a thermal energy distribution. The energy distribution of the sputtered aluminum particles decreases after its maximum accordingly to $\approx 1/E_n^2$ as expected from the theory [80,112].

It is well known that in sputtering also a kinetic energy input via fast neutrals which are produced by neutralization of backscattered ions may occur [28]. This contribution has been estimated by TRIM calculations, too. It depends strongly on the used sputter gas and target material. For the system Ar/Al at about 400 V, as it has been employed in the present case, the contribution of energetic backscattered argon atoms from the Al target is in the order of 0.2%. Therefore, we neglected this effect. However, in principle it has to be considered, for instance, in the case of copper sputtering where this influx might be in the order of 6% which is comparable to the other energetic parts.

The different contributions to the energy influx as described above are calculated for typical experimental conditions as used in magnetron sputtering and plotted versus the electron density in the substrate region in Fig. 36. Since the substrates are at floating potential, the energetic contributions of the charge carriers in comparison to the kinetic energy of the sputtered particles and the condensation energy of the film are rather low.

The total energy influx J_{in} has not only been calculated, it has also been measured with thermocouples. From the temporal change of the substrate temperature the integral deposited energy has been obtained by the method as described in Section 3.1. Fig. 37 shows two examples for the evolution of T_S at magnetron sputtering for different discharge power and target–substrate distances. When the plasma is switched on ($t = 0$) the integral energy influx J_{in} can be determined by taking the time derivative of T_S in Eq. (48). The experimental results for J_{in} at various deposition conditions are plotted in Fig. 38. Measured values of J_{in} (Fig. 38) are in excellent agreement with calculated values (Fig. 36). For instance, magnetron operation at 65 W and at a target–substrate distance of 14 cm corresponds to an electron density in the substrate region of $n_e = 3 \times 10^9\,\mathrm{cm}^{-3}$ and an aluminum growth rate of $W_{dep} = 1.1\,\mathrm{nm\,s}^{-1}$. Looking for the corresponding energy fluxes yield in each case $0.017\,\mathrm{J\,cm}^{-2}\,\mathrm{s}^{-1}$.

Surprisingly, the films sputtered onto small floating iron powder particles exhibit a rough, cauliflower-like structure compared to the smooth layers sputtered onto flat silicon wafers. The

Fig. 35. Simulation (a) and measurement (b) of the energy distribution of sputtered aluminum for a discharge voltage of 440 V.

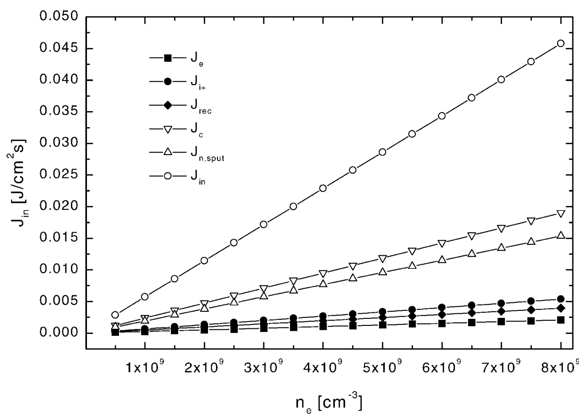

Fig. 36. Calculated contributions to the integral energy influx towards the substrate at magnetron sputtering ($V_s = V_{fl}$, $p = 1$ Pa).

difference is obvious if one compares the SEM micrograph of coated powder particles with the AFM picture of the aluminum film on silicon in Fig. 39. An essential reason for the observed differences in surface roughness might be the different substrate temperatures which are reached during the sputter process.

Although under comparable deposition conditions the energy influx towards a powder particle is the same as towards a flat substrate, the resulting temperature may be quite different. Due to much better heat conduction along the substrate holder ($J_{ext,2}$) the silicon substrate do not reach such high equilibrium temperatures as microscopic powder particles, which are mainly cooled by radiation ($J_{rad,2}$). Assuming an upper limit for the energy

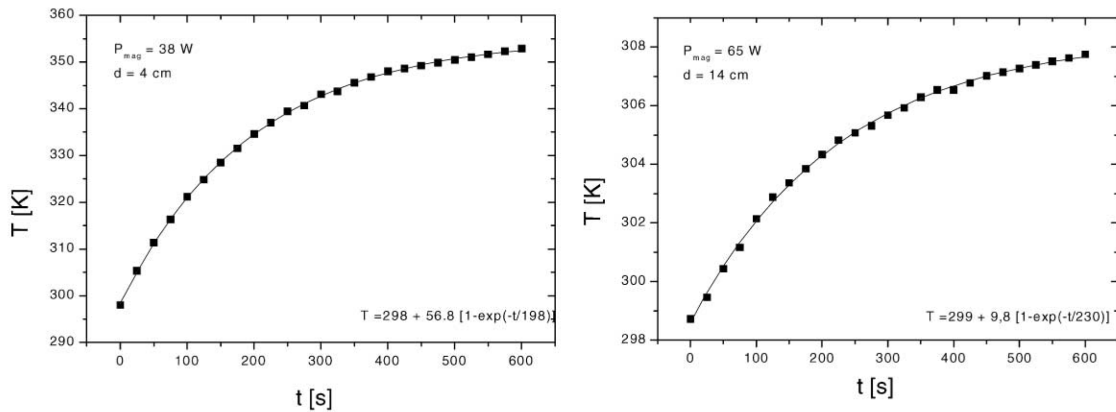

Fig. 37. Two examples for the evaluation of temperature of a silicon substrate heated during magnetron sputtering at different target–substrate distances and discharge power. Fit curves are according to Eq. (47).

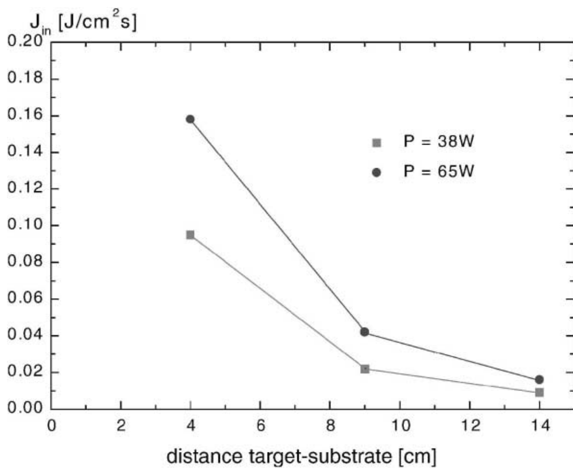

Fig. 38. Measured integral energy fluxes at magnetron sputtering of aluminum. The substrates were at floating potential.

influx of $0.2\,\mathrm{J\,cm^{-2}\,s^{-1}}$ which might be attained at high discharge power and low substrate–target distances the equilibrium temperature of a floating powder particle may reach values between 460 and 770 K. The first value is valid if one assumes a heat radiation emission coefficient of $\varepsilon = 0.9$, while the latter has been obtained for $\varepsilon = 0.1$.

In Table 3, the situation for the flat Si wafer and microscopic Fe particles is summarized. Especially for aluminum the effect of increasing grain size as the substrate temperature is increased, has been reported in literature [113].

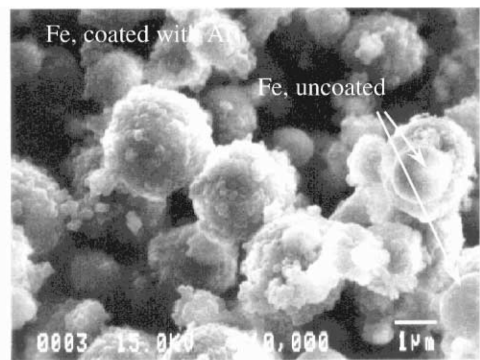

SEM picture of Al-coated Fe powder particles

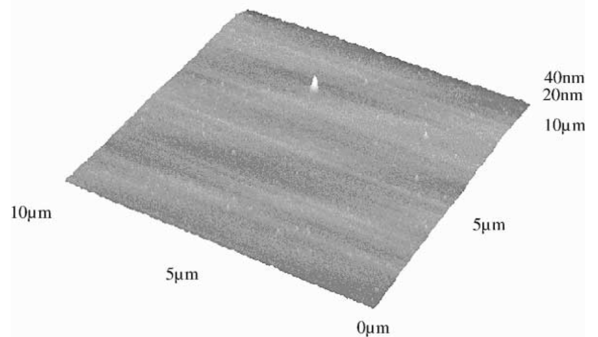

AFM picture of Al-coated Si substrate

Fig. 39. SEM micrograph of Al coated iron particles and reconstructed 3D plot of a sputtered Al film on silicon as examined by AFM. Although the films have been sputtered under the same plasma conditions there is a remarkable difference in the microstructure.

Table 3
Deposition of thin Al films onto Si substrates and Fe micro-particles

Substrate material:	Silicon wafer	Fe micro-particles
Substrate geometry:	large, flat	microscopic, spheric
Al film structure:	smooth	rough, cauliflower like
Energy loss:	$\dot{Q}_{out} = \int J_{ext,2}\, dA$	$\dot{Q}_{out} = \int J_{rad,2}\, dA$
Substrate temperature:	$\Delta T_S \approx 0$	$\Delta T_S \approx 0$

The experiments indicated that micro-disperse powder particles can be used as sensitive thermal probes in plasmas. This idea has been realized and successfully demonstrated in [114].

4.2. Plasma etching

4.2.1. The dependence of plasma etching on kinetic energy flux

In a similar manner as for the case in thin film deposition the energy flux and the substrate temperature play an important role in plasma etch processes.

For instance, Baggerman et al. [115] and Ding et al. [116] studied the influence of the energy influx J_{in} on the etching behaviour. Baggerman et al. could show that the ion-induced etching rate of organic polymers in argon and oxygen RF plasmas is proportional to the energy flux and appeared to be independent on pressure (Fig. 40). Since J_{in} depends only on the bombardment of energetic particles, it was concluded that the etch rate is completely determined by the impact of energetic neutrals and ions, and that the flux density of atomic and molecular oxygen (which is related to the pressure) is not the rate limiting quantity under these conditions.

Ding et al. obtained results for SiO_2 and Si etching in a CF_4/O_2/Ar-ECR plasma. The results may be generalized in order to characterize etching processes by energy fluxes and particle densities at the sheath edge. The experiments were performed in an electron cyclotron resonance (ECR) plasma. For both SiO_2 and Si etching the system parameters were varied in a wide range as follows: microwave power 500–900 W, pressure 0.1–0.5 Pa, DC self-bias of the wafer -25 to -100 V, and different gas mixtures consisting of CF_4, CF_4/O_2, CF_4/Ar with gas flow rates of 4.4–44 sccm. Ding et al. found that all experimental results could be included in a contour plot of the etch rate as a function of the ion energy flux ($J_{i,kin} = j_i E_{i,kin}$) and the atomic flourine density n_F, as can be seen in Fig. 41. The slope of the boundary line separating the etch behavior into two regimes gives a critical value for the ratio of $n_F/J_{i,kin}$. Above, the boundary line, i.e. $n_F/J_{i,kin}$ is larger than the critical value of 3.3×10^9 cm mW^{-1}, the etch rate increases linearly with the ion energy flux to the substrate and is independent on the atomic flourine density, see Fig. 42. That means the adsorption model is valid. Vice versa, below the boundary line in Fig. 41 the SiO_2 etch rate linearly increases with the atomic flourine density in the gas phase and is independent on the ion energy influx (Fig. 43). This case can be described by the flow-in model. It can be concluded that the ratio of reactive etch species to the energy influx (here $n_F/J_{i,kin}$) can be taken as a key parameter.

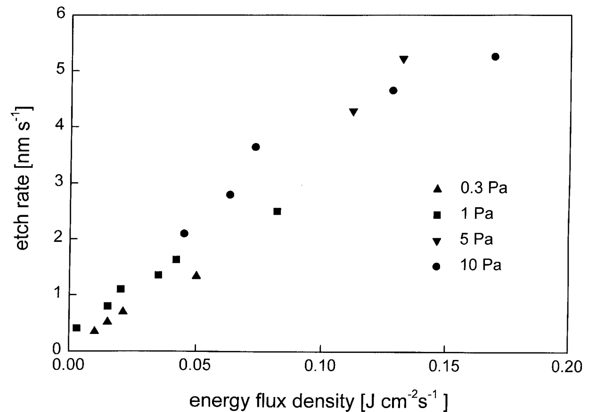

Fig. 40. The etch rate of photoresist in oxygen plasmas as a function of the energy flux density, from [115].

Qualitatively, the authors obtained similar results for Si etching as for SiO_2. However, the silicon etch rate shows in the energy flux limited regime a non-linear increase with the ion energy influx (see Fig. 44). This behavior might be explained by the competition between etching and polymerization process. Starting at ion energy fluxes in the order of about 100 mW cm^{-2} the deposition rate of fluorocarbon containing films increases with increasing energy flux, too.

Summarizing, one can register a proportional behavior of the etch rate with the energy flux J_{in}. This observation indicates that the process is dominated by chemical sputtering (CSP) as it has been described in Section 2.2.4.

For some etching systems the proportionally constants between etch rate and energy influx are given in Table 4. The low constants for polymer etching by argon is due to the fact that only physical sputtering appears, while the remarkably higher constants for etching with reactive gases can be explained by chemical reactions, i.e. ion enhanced chemical sputtering. It is evident, that comparison of the energy fluxes allows to facilitate process transfer between various etch reactors.

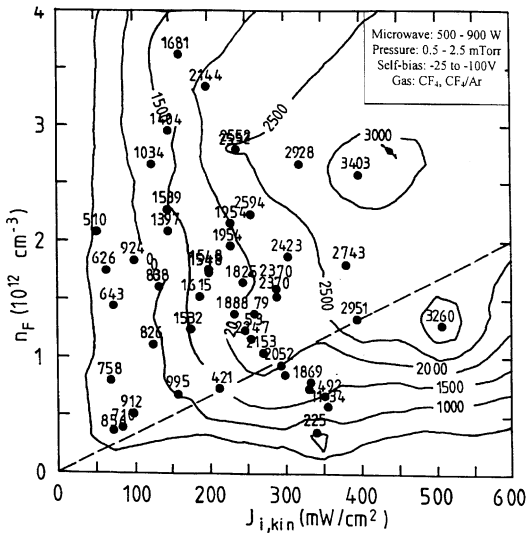

Fig. 41. Contour plot of SiO_2 etch rate (in A min^{-1}) as a function of the ion energy flux $J_{i,kin}$ to the substrate and of the atomic flourine density n_F in the plasma volume, from [116].

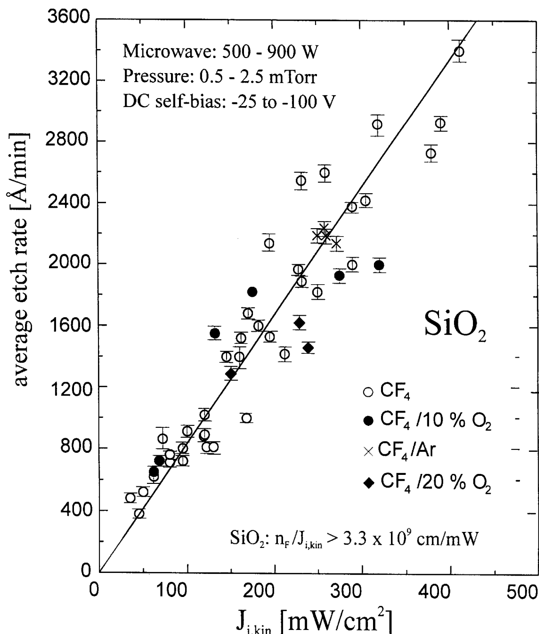

Fig. 42. Etch rate of SiO_2 vs. ion energy flux for $n_F/J_{i,kin} > 3.3 \times 10^9$ cm mW^{-1}, from [116].

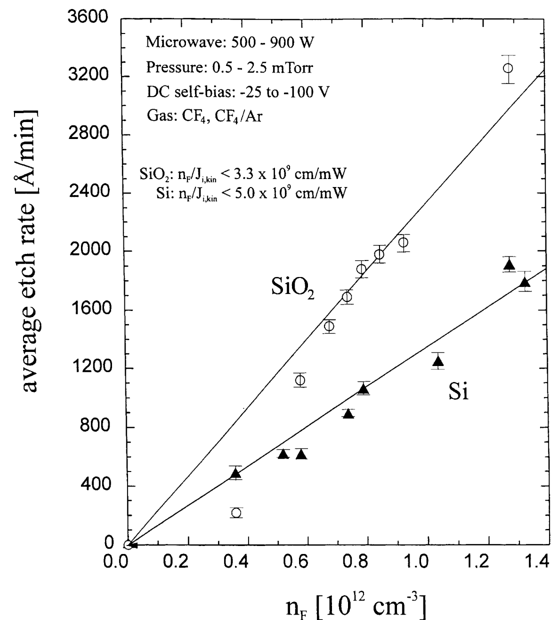

Fig. 43. SiO_2 and Si etch rates vs. atomic flourine density in the plasma volume for $n_F/J_{i,kin}$ lower than the critical value, from [116].

4.2.2. Importance of potential energy transfer in CF_4 glow discharge etching of silicon

In the following example we perform an experimental investigation on the energy transfer from an RF plasma to a silicon surface at CF_4 plasma etching [32]. The measurements will be explained on the basis of the formalism given in Section 2.1.2.

The total energy influx has been measured by the gradient method (see Section 3.1). The used substrate consisted of three silicon wafers glued together. In each of the two epoxy glue layers three thermocouples were mounted, see Fig. 45. This geometry allows us not only to study the surface temperature T_S, but also, by comparing the temperature in the two layers of epoxy, the heat flux ($\dot{Q}_{in}$) through the wafer. The plasma reactor has been described elsewhere [117]. It basically consists of a closed-geometry, planar RF discharge. The ion flux to the substrate was examined by energy-resolved mass spectrometry. The used process gases were CF_4 and Ar at flow rates of 20 and 40 sccm and at pressures of 50, 100, and 350 mTorr. The 13.56 MHz RF power was 20, 40, 60, or 80 W.

Depending on the etching conditions, the silicon substrate is heated by the plasma process. Fig. 46 shows an example of $T_S(t)$ for two different gases. From the measured initial slope $(dT_S/dt)_{t=0}$ the energy flux $\dot{Q}_{in} = \dot{Q}_S$ was determined (see Eq. (48)) by knowing the heat capacity of the sandwich wafer which was $C_S = 57\,\mathrm{J\,K^{-1}}$.

Under our conditions, radiation heating and heating by vibrational, rotational, and translational energy transfer can be neglected: separate experiments using infrared absorption spectroscopy have shown that the several associated temperatures (T_{vib}, T_{rot}, T_t) are nearly the same as the surface temperature T_S [117]. Therefore, we

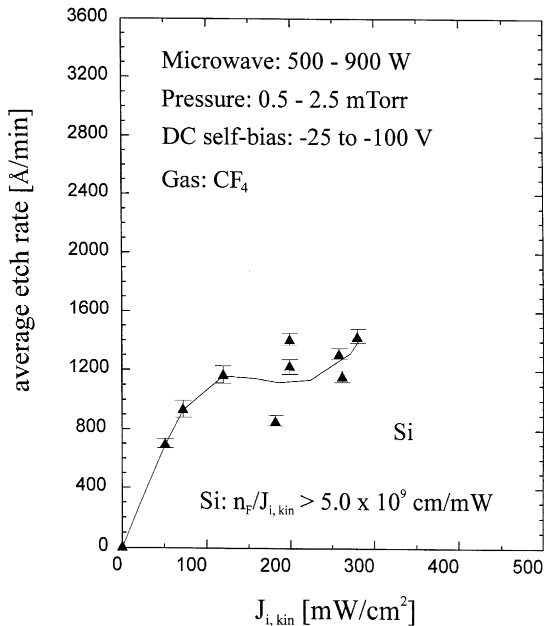

Fig. 44. Etch rate of Si in dependence on the ion energy flux to the substrate for $n_F/J_{i,kin} > 5 \times 10^9\,\mathrm{cm\,mW^{-1}}$, from [116].

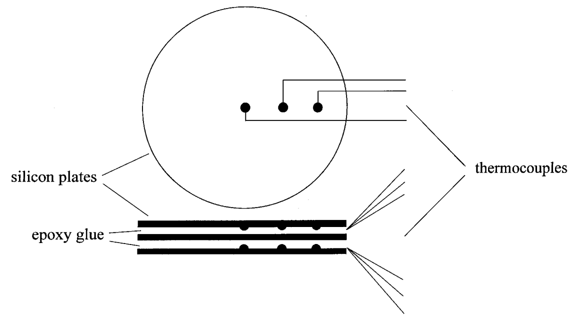

Fig. 45. Design of the silicon sandwich substrate.

Table 4
Some characteristic constants for different etching systems

System	Plasma	Etching component	Ref.	Const ($10^{-7}\,\mathrm{cm^{-3}/Ws}$)
Polymer film	Argon	Ar^+	[115]	6
Polymer film	Oxygen	O	[115]	37
SiO_2	CF_4	F, Ar^+	[116]	14,2
Si	CF_4	F, Ar^+	[116]	21,7

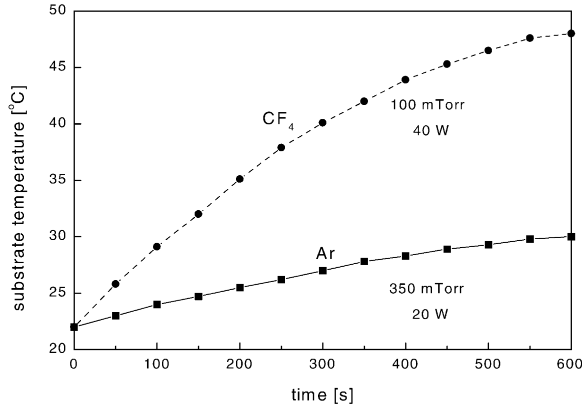

Fig. 46. Examples of the temporal evolution of substrate temperature induced by plasma ion bombardment.

can restrict ourselves to the analysis of the heating of the Si surface only by ion bombardment.

The energy $\dot{Q}_{in}$ supplied by the ions to the substrate consists of a potential and a kinetic contribution:

$$\dot{Q}_{in} = j_i A_S(\kappa_{i,pot}E_{i,pot} + \kappa_{i,kin}E_{i,kin}), \tag{67}$$

where j_i denotes the ion flux, A_S the substrate area (79 cm^2), $E_{i,pot}$ and $E_{i,kin}$ the potential and kinetic energy of the impinging ions, respectively; $\kappa_{i,pot}$ and $\kappa_{i,kin}$ are the corresponding energy transfer coefficients, which are related to coefficients introduced in Eq. (11). Under our discharge conditions the ion flux j_i is determined by the Bohm criterion [107].

The potential energy $E_{i,pot}$ is closely related to the ionization potential E_{ion}. The kinetic energy $E_{i,kin}$ must be measured or calculated. The transfer coefficients as introduced in Eq. (6) and Eqs. (11)–(13) can be now also expressed as

$$\kappa_{i,pot} = 1 - \frac{\Phi}{E_{ion}} - \gamma_i\frac{\Phi + E_{i,kin}}{E_{ion}} = \frac{E_{i,pot}}{E_{ion}} \tag{68}$$

and

$$\kappa_{i,kin} = \delta = 4k_c\frac{M_1M_2}{(M_1 + M_2)^2}(\sin\theta/2)^2, \tag{69}$$

where M_1, M_2 are the atomic masses of the colliding particles, θ is the angle of incidence of ions, and k_c is the kinetic energy transfer efficiency.

The interpretation of the substrate heating by ion bombardment requires the knowledge of $E_{i,kin}$, n_i, and kT_e. The mean kinetic energy $E_{i,kin}$ was determined by plasma monitoring. The dominant ion in the CF_4 discharge was found to be CF_3^+. The electron density and electron temperature, which are necessary for the calculation of the ion flux by the Bohm equation, were obtained by microwave resonance spectroscopy and laser-induced photodetachment [117]. The required values for E_{ion}, Φ, and γ_i were taken from the literature [31].

In Table 5, all experimental conditions and derived physical quantities are summarized.

In Fig. 47, which can be obtained from Table 4, the calculated value $J_{i,kin}$, which is equivalent to the (uncorrected) kinetic energy transfer from ions to surface, is plotted versus the energy $\dot{Q}_S$ absorbed by the substrate. The relation appears to be roughly linear. Because of the transfer of potential (=ionization) energy to the surface the line does not pass through zero.

Another result which can be drawn from Table 5 is the kinetic energy transfer efficiency δ (see Eq. (67)) [32]

$$\delta = \kappa_{i,kin} = \frac{\dot{Q}_S - j_iA_S\kappa_{i,pot}E_{i,pot}}{j_iA_SE_{i,kin}}. \tag{70}$$

In Fig. 48, the transfer efficiency $\kappa_{i,kin}$ is plotted as a function of the average kinetic energy of the ion bombardement ($E_{i,kin}$). The value of $\kappa_{i,kin}$ ranges between 0.5 and 1, with a tendency to increase for lower energies. This is in perfect agreement with data reported by Winters et al. [30] for the low-energy regime.

We would like to conclude that the heating of a silicon substrate due to exposure to a CF_4–RF–plasma is primarily caused by the bombardment with CF_3^+ ions, where both the kinetic and potential energy transfer has to be taken into account.

4.2.3. Ions and chemical reactions as heat sources in plasma cleaning of metal surfaces contaminated with lubricants

Plasma cleaning of metals belongs to the most important applications of non-isothermal plasmas in dry surface processing [118–120]. If integrated into a production line, cleaning and surface activation by plasma can be an efficient, reliable,

Table 5
Measured and calculated quantities for a few experimental conditions at RF plasma etching in Ar/CF_4

Experimental conditions	n_{i+} (cm^{-3})	$E_{i,kin}$ (eV)	(dT_S/dt) ($K\,s^{-1}$)	J_i ($cm^{-2}s^{-1}$)	$j_i\kappa_{i,pot}E_{i,pot}A_S$ ($J\,s^{-1}$)	$j_iE_{i,kin}A_S$ ($J\,s^{-1}$)	$\dot{Q}_s$ ($J\,s^{-1}$)
CF_4, 20 sccm 50 mTorr 20 W	6.2×10^9	42	2.0×10^{-3}	7.6×10^{14}	0.035	0.17	0.114
CF_4, 20 sccm 100 mTorr 20 W	5.1×10^9	40	2.1×10^{-3}	6.2×10^{14}	0.029	0.13	0.120
CF_4, 20 sccm 100 mTorr 40 W	8.2×10^9	52	3.8×10^{-3}	10.0×10^{14}	0.044	0.27	0.217
CF_4, 20 sccm 100 mTorr 60 W	13.2×10^9	57	5.6×10^{-3}	15.9×10^{14}	0.067	0.48	0.320
CF_4, 20 sccm 100 mTorr 80 W	19.1×10^9	65	8.5×10^{-3}	23.2×10^{14}	0.093	0.80	0.486
Ar, 40 sccm 350 mTorr 20 W	1.8×10^9	15	1.1×10^{-3}	2.8×10^{14}	0.036	0.022	0.063

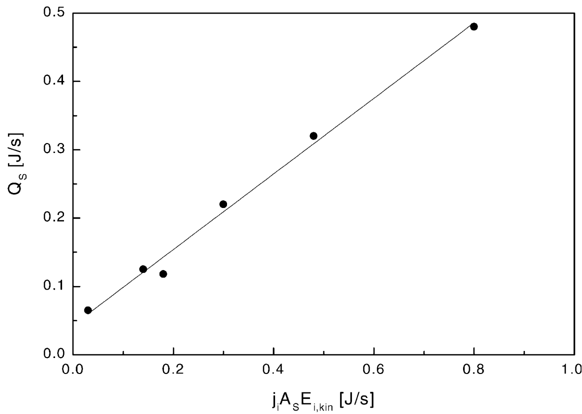

Fig. 47. Energy needed to heat the substrate ($\dot{Q}_S$) as a function of the kinetic ion energy which the plasma offers to the silicon surface.

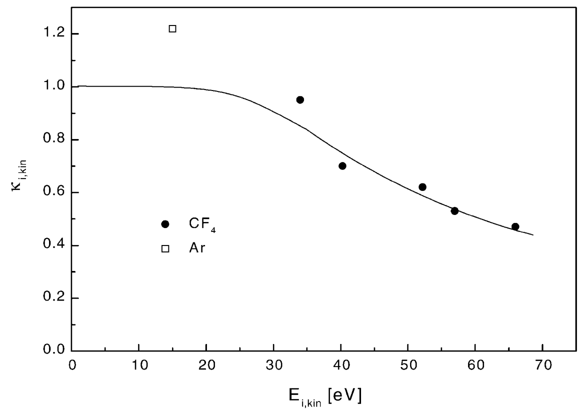

Fig. 48. The kinetic energy transfer efficiency $\kappa_{i,kin}$ as a function of the mean kinetic energy of the ions.

and non-polluting pretreatment for painting. In the plasma cleaning experiments presented here aluminum plates which are contaminated with hydrocarbon containing compounds (lubricants) were treated in an O_2-plasma generated by a DC-discharge [121,122].

The surface cleaning via physical (PS) and chemical sputtering (CS) leads to a bombardment of the substrate by ions which causes an immediate surface purification, but also a rather high-energy influx. Thus, the substrates are heated to a certain extent during the sputter process. Also the heat released in exothermic surface reactions (SFR) as the combustion of lubricants influences the thermal balance at the surface [68].

A schematic view of the experimental setup used for plasma cleaning is given in Fig. 49. A detailed description of the experiments and their results in regard to the efficiency of the cleaning process as

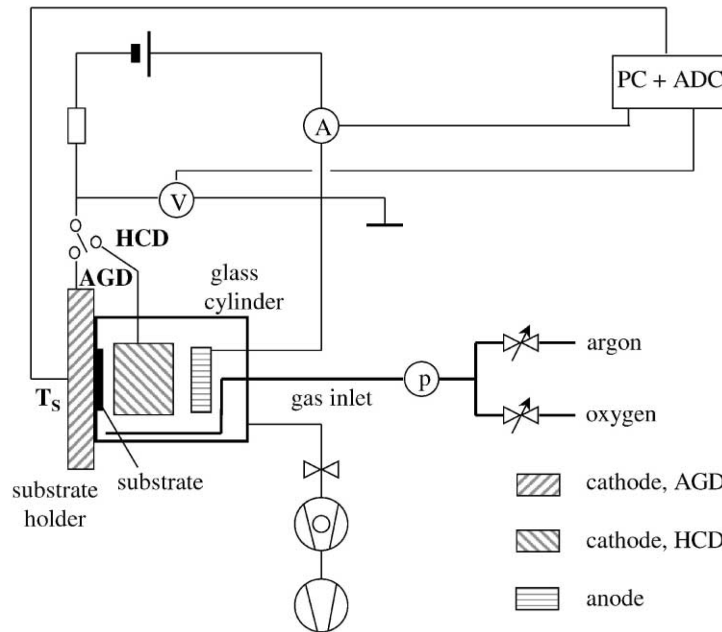

Fig. 49. Experimental set-up for plasma cleaning.

well as concerning the process monitoring may be found elsewhere [68]. The substrates which have been contaminated aluminum plates were clamped on a sample holder. The holder consists of a large aluminum disk with a high heat capacity for an effective cooling of the substrates during plasma treatment. As contamination served Wisura–Akamin which is a typical lubricant in handling and industrial treatment of aluminum sheet metals. Akamin is a petroleum-like light lubricant distillate of about 90% continuous-chain alcanes. The initial thickness of the lubricant film estimated from spectroscopic ellipsometric measurements were between 50 and 150 nm.

The macroscopic discharge parameters as power and pressure have been varied between 5 and 80 W (power density: 0.2–4 W cm^{-2}) and 10–20 Pa, respectively. The power density as mentioned here describes the discharge power per cathode area. During the plasma treatment (1–15 min) the substrate temperature could reach values between 20°C and 150°C.

Besides a variation of the macroscopic discharge parameters two different discharge modes have been studied in order to verify the effect of ions: the anomalous glow discharge regime (AGD) where the contaminated substrate served as cathode and the hollow cathode discharge regime (HCD) where the substrate was not at cathode potential but at floating potential. The choice of the discharge mode could be simply realized by switching between the two cathodes (Fig. 49). In the AGD regime the sample holder on which the substrates have been mounted was operated as cathode. The anode was an aluminum ring placed above the cathode disk. The voltage between the electrodes was varied between 500 and 1200 V. The discharge has been observed as very homogeneous.

In the so-called HCD mode a cubus-shaped hollow metal piece served as cathode. This cathode was placed immediately in front of the sample holder with the substrate to be treated. The anode ring was the same as mentioned above. Again the discharge voltage could be varied in a similar range as in the AGD.

In the AGD regime the ions generated in the negative glow play an important role. They are accelerated in the cathode fall in front of the contaminated substrate and get a kinetic energy in the order of some hundreds eV. Under these

conditions a combined action of chemically activated species and a bombardment of the substrate by high-energetic ions has been realized. Vice versa, in the HCD regime the ions got only the energy difference of some eV between plasma and floating potential of the substrate. In that case the surface cleaning proceeds only by the chemically reactive oxygen radicals. Since the plasma conditions in both discharge modes are comparable, however, the substrate acts as cathode in the AGD, but as a part of the wall in HCD the influence of the ionic and chemical contributions could be separated quite well.

The temperature of the substrates have been monitored by using thermocouples and the integral energy influx was determined from the temperature raise ($\mathrm{d}T_S/\mathrm{d}t$) at $t = 0$, see Section 3.1. Simultaneously to the temperature measurements the cathode fall thickness (sheath) d_{sh} and the bias-voltage V_{bias} have been determined to get a rough estimation of the ion energy and ion flux density.

A typical example of the evolution of the temperature at the substrate surface during plasma cleaning in an anomalous oxygen glow discharge is plotted in Fig. 50. The heating curve was obtained at an oxygen pressure of 18 Pa, a power density of $1.3\,\mathrm{W\,cm^{-2}}$, and a plasma treatment time of 5 min. When the plasma is ignited ($t = 0$) the integral energy flux $\dot{Q}_{in}$ can be obtained by taking the time derivative of T_S, see also Eq. (48):

$$\left(\frac{\mathrm{d}T_S}{\mathrm{d}t}\right)_{t=0} = \frac{\dot{Q}_{in}}{d_S A_S \varrho c_S}. \tag{71}$$

For the used aluminum substrate ($\varrho = 2.7\,\mathrm{g\,cm^{-3}}$, $c_S = 0.92\,\mathrm{J/gK^{-1}}$, $d_S = 0.2\,\mathrm{cm}$, $A_S = 25\,\mathrm{cm^2}$) and under the experimental conditions given above an energy influx of $\dot{Q}_{in} = 7.5\,\mathrm{J\,s^{-1}}$ could be determined.

The obtained energy influxes in dependence on the power density for AGD and HCD are plotted in Fig. 51. It is obvious that the energy influx towards the aluminum substrates during plasma cleaning in the anomalous glow discharge is larger than in the hollow cathode mode. The contribution of the exothermic reaction heat by the combustion of the hydrocarbon containing lubricant layers by oxygen species is nearly the same in both cases. However, in the AGD mode the ions are accelerated towards the cathode (substrate) where they receive a maximum of kinetic energy.

As mentioned above, the total energy influx $\dot{Q}_{in}$ consists of a contribution by the exothermic chemical reactions ($J_{react,1}$) and a contribution of the ions ($J_{i,kin}$):

$$\begin{aligned}\dot{Q}_{in} &= \int (J_{react,1} + J_{i,kin})\,\mathrm{d}A \\ &= \int (j_{react}E_{react} + j_i E_{i,kin})\,\mathrm{d}A.\end{aligned} \tag{72}$$

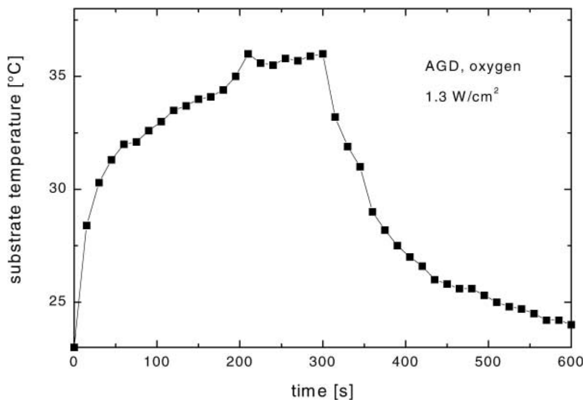

Fig. 50. An example for a measured time-dependent temperature curve $T_S(t)$, obtained at the plasma cleaning of lubricant-contaminated aluminum (18 Pa).

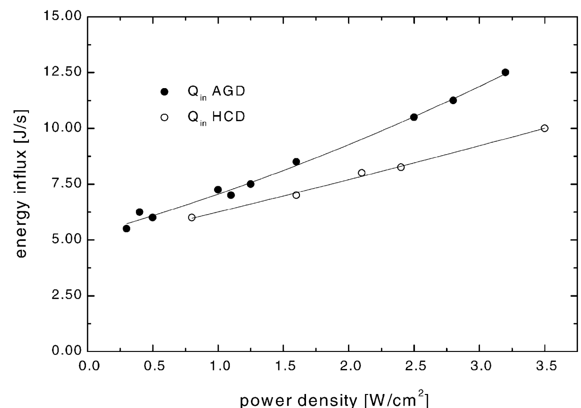

Fig. 51. Total energy influx during plasma cleaning determined for HCD and AGD.

The contribution due to chemical reactions which is about the same in both the AGD and the HCD mode can be calculated by the product of the average energy E_{react} released per combustion reaction of a lubricant molecule with the particle flux density j_{react} of the reactive oxygen atoms. The total oxygen atom flow density j_{react} depends on the oxygen dissociation degree which is in the order of $x_D \approx 0.01-0.05$ under our experimental conditions, on the volume density of O_2-molecules (N_{O_2}) and on the gas temperature T_g:

$$j_{react} = \frac{1}{4} x_D N_{O_2} \sqrt{\frac{8kT_g}{\pi m_{O_2}}} = \frac{x_D p_{O_2}}{4kT_g} \sqrt{\frac{8kT_g}{\pi m_{O_2}}}. \quad (73)$$

For a gas pressure of $p_{O_2} = 18\,\text{Pa}$ and a gas temperature of about $T_g = 400\,\text{K}$ we obtain for the inflow of oxygen atoms towards the substrate in the order of $j_{react} = 0.5\text{–}2.5 \times 10^{18}\,\text{cm}^{-2}\,\text{s}^{-1}$. The surface density of bulk atoms and of the contamination layer, too, is in the order of 10^{14}–$10^{15}\,\text{cm}^{-2}$. Thus, the relatively high particle influx results in rather fast surface reactions of contaminations with oxygen even if the sticking probability of the reactive atoms at the contaminated surface should be small. The reaction products desorb either thermally or via sputtering if bombarded with charge carriers.

The used lubricants are mainly mixtures of long-chain alcanes as nonane, decane, and undecane. The combustion heat of the lubricant has been determined experimentally to be about $45\,\text{kJ}\,\text{g}^{-1}$. Assuming a mean molar mass of $142\,\text{g}\,\text{mol}^{-1}$ for the lubricant we get a reaction enthalpy of $6400\,\text{kJ}\,\text{mol}^{-1}$. Dividing the reaction enthalpy by Avagadros number we obtain the heat E_{react} released by the complete combustion of a lubricant molecule with oxygen to CO_2 and H_2O:

$$E_{react} = \frac{6400\,\text{kJ}\,\text{mol}^{-1}}{6 \times 10^{23}\,\text{mol}^{-1}} \approx 10^{-17}\,\text{J}. \quad (74)$$

Since for such a complete reaction a lot of oxygen atoms are necessary, this number has to be taken into account at the particle flux density. Under these assumptions, we obtained an estimated value for $J_{react,1}$ of $0.15\text{–}0.8\,\text{J}\,\text{cm}^{-2}\,\text{s}^{-1}$, which yields a maximum energy influx of $\dot{Q}_{react} = 4-20\,\text{J}\,\text{s}^{-1}$ by exothermic reactions of the lubricants with plasma generated oxygen atoms at the contaminated substrate surface.

The energy influx $\dot{Q}_{in}$ measured under HCD conditions is in the range of $6\text{–}10\,\text{J}\,\text{s}^{-1}$ increasing with discharge power density which was varied between 0.8 and $3.5\,\text{W}\,\text{cm}^{-2}$. The calculated energy influx by chemical reactions is in the same order. However, because a certain energy loss by desorption of the products (CO_2, H_2O) has been neglected the theoretically estimated values are higher than the experimentally obtained. The radical density raises weakly with increasing supplied power because of a higher rate by electron impact dissociation resulting in an improved efficiency of chemical surface cleaning. In the range studied the degree of dissociation increases by the factor of two.

In order to calculate the energy influx $J_{i,kin}$ by the ions striking the aluminum substrate it was necessary to know the ion particle flux (j_i) to the substrate surface and the mean kinetic energy ($E_{i,kin}$) of the oxygen ions. The kinetic energy $E_{i,kin}$ was calculated by the ion energy distribution function $f(V)$ by integration from zero up to the bias potential V_{bias}. The ion energy distribution function (IEDF) has been calculated roughly by using an analytic expression for $f(V)$ [41]:

$$f(V) = \frac{1}{1 - \exp(-d_{sh}/\lambda)} \frac{1}{2} \frac{1}{V_{bias}} \frac{d_{sh}}{\lambda} \frac{1}{\sqrt{1 - V/V_{bias}}} \times \exp\left(-\frac{d_{sh}}{\lambda}\left(1 - \sqrt{1 - V/V_{bias}}\right)\right). \quad (75)$$

($\dot{d}_{sh}$ the thickness of the sheath (cathode fall), λ the mean free path of the ions.)

In the anamolous glow regime the bias voltage V_{bias} is roughly given by the cathode potential, whereas in the hollow cathode regime it is only in the order of the floating potential.

But only a part of the kinetic ion energy will be transferred to the substrate due to collision processes as discussed in Section 2.1.2.

The maximum flux density of the oxygen ions j_i was determined by Child's law as indicated in Eq. (14). The calculated current density is comparable with the measured ones under the assumption that the current at the cathode is only carried by the ions.

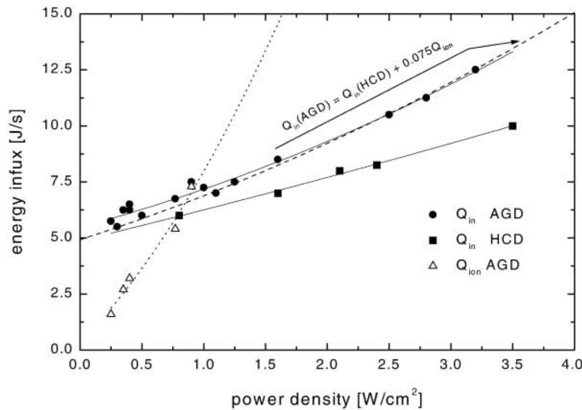

Fig. 52. Energy influx by the ions: ⋯ theoretically possible, – – really transferred.

The values of $J_{i,kin}$ which have been calculated as described above are compared with the measured influxes as plotted in Fig. 52. One can recognize that the theoretically estimated energy influx by the ions is much larger than the experimentally determined contribution which can be obtained by the difference of the energy influxes in the AGD and the HCD mode. This is due to the assumption of maximum values for the energy transfer, that means the maximum of possible mean kinetic energy and ion particle flux. Only about 7.5% of this maximum possible ion energy is really transferred towards the surface. However, the importance of the ions in regard to plasma surface cleaning is not only for substrate heating. Moreover, the ions are the essential component to increase the etching rate of the lubricant films by ion enhanced reactions, sputtering, etc. Even a relatively small portion of charge carriers may change the etching behavior in a drastic manner. For instance, an ion bombardment of the layer under treatment influences the break of chemical bonds of large lubricant molecules and stoichiometric changes at the surface.

5. Summary

The energy influx towards the surface is one of the most important properties of plasma–wall interaction for comparing and scaling-up several plasma processes.

In the first part of this article we have described how the various contributions to the energy balance of a plasma-exposed solid surface can be determined in general. When analyzing the thermal behavior of an experimental system, all contributions should be estimated. The smallest ones can be neglected. Vice versa, by knowing the temporal and spatial evolution of the surface temperature and therefore of the thermal conditions at the solid surface during plasma treatment one can obtain information on the energy fluxes and their transfer mechanisms which have been taken place and which determine these thermal conditions.

In the second part of the review we discussed in more detail some typical examples of plasma systems of technological importance as thin film deposition and plasma etching.

Acknowledgements

This study was supported by the Deutsche Forschungsgemeinschaft under SFB 198, by the NATO (CRG 910895), and the Dutch Alexander von Humboldt stichting. The authors would like to thank J. Schulze, R.J.J.M. Snijkers, J.F. Behnke, and H. Wulff for their support.

References

[1] Thornton JA. J Vac Sci Technol 1974;11:666.
[2] Hussla B, Enke K, Grunwald H, Lorenz G, Stoll H. J Phys D Appl Phys 1987;20:889.
[3] Deutsch H, Kersten H, Rutscher A. Contrib Plasma Phys 1989;29:263.
[4] Deutsch H, Kersten H, Klagge S, Rutscher A. Contrib Plasma Phys 1988;28:149.
[5] Zubimendi JL, Vela ME, Salvarezza RC, Vazquez C, Vara J, Arvia AJ. Phys Rev E 1994;50:1367.
[6] Bernstein SD, Wong TY, Tustison RW. J Vac Sci Technol B 1994;12:605.
[7] Kugler S, Shimakawa K, Watanabe T, Hayashi K, Laszlo I, Bellissent R. J Non-Cryst Solids 1993; 164–166:1143.
[8] Bang K, Ghajar AJ, Komanduri R. Thin Solid Films 1994;238:172.

[9] Savaloni H, Player MA, Gu E, Marr GV. Rev Sci Instrum 1992;63:1497.
[10] Brune H, Roder H, Bromann K, Kern K. Thin Solid Films 1995;264:230.
[11] Windischmann H. J Appl Phys 1987;62:1800.
[12] Rossnagel SM. Thin Solid Films 1989;171:143.
[13] Muller KH. Appl Phys A 1986;40:209.
[14] Nimmagadda R, Bunshah RF. J Vac Sci Technol 1971;8:677.
[15] Chow R, Bunshah RF. J Vac Sci Technol 1971;8:665.
[16] Thornton JA. Thin Solid Films 1978;54:23.
[17] Magunor A. Instr and Experimental Techn 2000;2:3.
[18] Rapakoulias DE, Gerassimou DE. J Appl Phys 1987;62:402.
[19] Cardinaud C, Peignon MC, Turban G. Proceedings ISPC-11, Loughborough, 1993. p. 1505.
[20] Steffen H, Kersten H, Wulff H. J Vac Sci Technol A 1994;12:2780.
[21] Kersten H, Steffen H, Vender D, Wagner HE. Vacuum 1995;46:305.
[22] Dupret F, Nicodeme P, Ryckmans Y, Wouters P, Crochet MJ. Int J Heat Mass Transfer 1990;33:1849.
[23] Dey SK, Delahoy AE, Anderson WA. J Vac Sci Technol 1978;14:1739.
[24] Sevastyanenko VG, Liping GU, Bakken JA. Proceedings of the 12th ISPC, Minneapolis, 1995. p. 2357.
[25] Leroy O, Perrin J, Jolly J, Pealat M, Lefebvre M. J Phys D: Appl Phys 1997;30:499.
[26] Piejak R, Godyak V, Alexandrovich B, Tishchenko N. Plasma Sourc Sci Technol 1998;7:590.
[27] Tatarova E, Stoykova E, Bachev K, Zhelyazkov I. IEEE Trans Plasma Sci 1998;26:167.
[28] Andritschky M, Guimaraes F, Teixeira V. Vacuum 1993;44:809.
[29] Wendt R, Ellmer K, Wiesemann K. J Appl Phys 1997;82:2115.
[30] Winters HF, Horne D. Phys Rev B 1974;10:55.
[31] Handbook of chemistry and physics. (73rd ed.) Boca Raton, FL: CRC Press, 1992/93.
[32] Kersten H, Snijkers RJMM, Schulze J, Kroesen GMW, Deutsch H, de Hoog FJ. Appl Phys Lett 1994;64:1496.
[33] Emeleus KG, Coulter JRM. Il Nuovo Cimento 1986;7D:79.
[34] Behnke JF, Bindemann T, Deutsch H, Becker K. Contrib Plasma Phys 1997;37:345.
[35] Daugherty JE, Graves DB. J Vac Sci Technol A 1993;11:1126.
[36] Schwarzenbach W, Howling AA, Fivaz M, Brunner S, Hollenstein C. J Vac Sci Technol A 1996;14:132.
[37] Zeuner M, Neumann H, Meichsner J. J Appl Phys 1997;81:2985.
[38] Snijkers RJMM. Ph.D. thesis, TU Eindhoven, 1993.
[39] Vender D, Boswell RW. IEEE Trans Plasma Phys 1990;18:925.
[40] Snijkers RJMM, van Sambeck, Kroesen GMW, deHoog FJ. Appl Phys Lett 1993;63:308.
[41] Davies WD, Vamderslice TA. Phys Rev 1963;131:219.
[42] Tandian NP, Pfender E. Plasma Chem Plasma Proc 1997;17(3):353.
[43] Visser RJ. J Vac Sci Technol A 1989;7:189.
[44] Ingram SG, Braithwaite NS. J Phys D: Appl Phys 1988;21:1496.
[45] Stoffels E, Stoffels W. Ph.D. thesis, TU Eindhoven, 1994.
[46] Klagge S, Tychi M. Czech J Phys B 1985;35:988.
[47] Woodworth JR, Riley ME, Meister DC, Aragon BP, Le MS, Sawin HH. J Appl Phys 1996;80:1304.
[48] Suzuki T, Kasayu T. Phys Rev A 1987;36:2129.
[49] Tychi M, Kudrna P, Behinke JF, Csambal C, Klagge S. J Phys IV 1997;7:C4-397.
[50] Adler F, Kersten H, Steffen H. Contrib Plasma Phys 1995;35:213.
[51] Kersten H, Stoffels E, Stoffels W, Otte M, Csambal C, Deutsch, H, Hippler R. J Appl Phys 2000;87:3637.
[52] Winkler R, Petrov G, Sigeneger F, Uhrlandt D. Plasma Sources Sci Technol 1997;6:118.
[53] Ventzek PLG, Hoekstra, Kushner MJ. J Vac Sci Technol B 1994;12:461.
[54] Boswell RW, Morey IJ. Appl Phys Lett 1988;52:21.
[55] Kersten H, Kroesen GMW, Hippler R. Thin Solid Films 1998;332:282.
[56] Asscher M, Guthrie WL, Lin TH, Somorjai GA. J Chem Phys 1983;78:6992.
[57] Doshita A, Ohtani K, Namiki A. J Vac Sci Technol A 1998;16:265.
[58] Kawano H, Funato K, Maeda T, Zhu Y. Appl Surf Sci 1997;119:341.
[59] Kupfer H, Ackermann E, Schaarschmidt G, Scholze F, Wallendorf T, Hecht G. Wiss Z Uni Chemnitz 1991;4:12.
[60] Krebs K. Phys 1936;101:604.
[61] Phillips MH, Anderson LW, Lin CC, Meers RE. Phys Lett 1981;82A:404.
[62] Magunov A. Plasma Phys Rep 1997;23:940.
[63] Sigmund P. In: Behrisch R, editor. Sputtering by particle Bombardment I. Berlin: Springer, 1981. p. 9.
[64] Eckstein W, Biersack JP. Z Physik 1986;B63:471.
[65] Cooks RG. Org Mass Spectrom 1993;28:1021.
[66] Kersten H, Kroesen GMW. J Vac Sci Technol 1990;A8:38.
[67] Durandet A, Joubert O, Pelletier J, Pichot M. J Appl Phys 1990;67:3862.
[68] Kersten H, Deutsch H, Behnke JF. Vacuum 1997;48:123.
[69] Halpern B, Rosner DE. J Chem Soc Faraday Trans 1978;174:1883.
[70] Bonzel HP, Ku R. Surf Sci 1972;33:91.
[71] Eley DD. Chem Ind(1) 1976;12.
[72] Daviet JF, Peccoud L, Mondon F. J Appl Phys 1993;73:1471.
[73] Knudsen M. Ann Phys (Leipzig) 1911;34:593.
[74] Wilbers ATM, Meeusen GJ, Haverlag M, Kroesen GMW, Schram DC, Kersten H. Thin solid films 1991;204:59.
[75] Vanselow R, Howe R, editor. Chemistry and physics of solid surfaces IV. Berlin: Springer, 1983. p. 389.
[76] Somorjai GA. Introduction to surface chemistry and catalysis. New York: Wiley, 1994.
[77] Moraw M. Vacuum 1986;36:523.

[78] Wittkopf H. Vacuum 1987;37:819.
[79] Lee HJ, Choi JG, Colling CW, Mudholkar MS, Thompson LT. Appl Surf Sci 1995;89:121.
[80] Roth J. In: Post DE, Behrisch R, editors. Physics of plasma–wall interactions in controlled fusion, Vol. 131. NATO ASI Series p. 351.
[81] Champion RL, Tucek JC. In: Babucke G, editor. Proceedings of GD'97, Greifswald, 1997. p. 649.
[82] Baggerman JAG, Visser RJ, Collart EJH. Proceedings, ISPC-11, Loughborough, 1993. p. 1410.
[83] Kersten H, Kroesen GMW. Contrib Plasma Phys 1990;30:725.
[84] Thornton JA, Lamb JL. Thin Solid Films 1984;119:87.
[85] Magunov AN. Plasma Phys Rep 1997;23:940.
[86] Oakes DB, Butler JE, Snail KA, Carrington WA, Hanssen M. J Appl Phys 1991;69:2602.
[87] Lapierre D, Kearney RJ, Vardelle M, Vardelle A, Fauchais P. Plasma Chem Plasma Proc 1994;14:407.
[88] Dohnalek Z, Mezhenny S, Lyubinetsky I, Choyke WJ, Yates JT. J Vac Sci Technol 1997;A15:2766.
[89] Hosokawa A, Kowaka M. J Vac Sci Technol B 1996;14:494.
[90] Huang C, Lang M, Brueck SRJ. J Vac Sci Technol 1996;14:271.
[91] Kroesen GMW, Oehrlein GS. Bestwick TD J Appl Phys 1991;69:3390.
[92] Donelly VM. In: Glocker DA, Shah SI, editors. Handbook of thin process technology, Bristol and Philadelphia: IOP, 1995.
[93] Lukin OV, Magunov AN. SPIE 1994;2321:439.
[94] Kikichi J, Fujimura S, Kurosaki R, Yano H. J Vac Sci Technol 1997;A15:2035.
[95] Magunov AN. Sov Tech Phys Lett 1992;18:317.
[96] Magunov AN, Lukin OV. Russ Microelectron 1996;25:97.
[97] Berger R, Gerber C, Gimzewski JK, Meyer E, Gntherodt H. J Appl Phys Lett 1996;69:40.
[98] Shindo W, Ohmi T. J Appl Phys 1996;79:2347.
[99] Thornton JA. J Vac Sci Technol 1974;11:666.
[100] Mirkarimi PB, McCarty KF, Medlin DL, Wolfer WG, Friedmann TA, Klause EJ, Cardinale GF, Howitt DG. J Mater Res 1994;9:2925.
[101] Grossmann E, Lampert GD. Appl Phys Lett 1996;68:1214.
[102] Deutsch H, Schmidt M. Beitr Plasmaphys 1981;21:279.
[103] V. Keudell A, Miller W. J Appl Phys 1994;75:7718.
[104] Kroesen GMW, Timmermans CJ, Schram DC. Pure Appl Chem 1988;60:795.
[105] Yoon SF, Yang H, Rusli J, Ahn J, Zhang Q, Poo TL. Diamond Relat Mater 1997;6:1683.
[106] Lunk A. Vacuum 1990;41:1965.
[107] Bohm D. In: Guthrie A, Wakerling RK, editor. The characteristics of electrical discharges in magnetic fields. New York, 1949.
[108] Margreiter D, Deutsch H, Maerk TD. Int J Mass Spectr 1994;139:127.
[109] Steffen H, Wulff H. Thin Solid Films 1995;263:18.
[110] Kersten H, Schmetz P, Kroesen GMW. Surf Coatings Technol 1998;108–109:493.
[111] Klick M. J Appl Phys 1996;79:3445.
[112] Robinson MT. Philos Mag 1968;17:639.
[113] Glocker DA, Shah SI, Editor. Handbook of thin film. Proceedings Technology (X2), IOP, 1995.
[114] Swinkels GHPM, Kersten H, Deutsch H, Kroesen GMW. J Appl Phys 2000;88:1747.
[115] Baggerman JAG, Visser RJ, Collart EJH. J Appl Phys 1994;75:758.
[116] Ding J, Jenq JS, Kim KH, Maynard HL, Hamers JS, Hershkowitz N, Taylor JW. J Vac Sci Technol 1993;A11:1283.
[117] Haverlag M. Ph.D. thesis, TU Eindhoven, 1991.
[118] Dylla HF. J Vac Sci Technol 1988;A6:1276.
[119] Korzec D, Rapp J, Theirich D, Engemann J. J Vac Sci Technol 1994;A12:369.
[120] Holland L. Vacuum deposition of thin films. London: Chapman & Hall, 1958, p. 74.
[121] Kersten H, Behnke JF, Eggs C. Contrib Plasma Phys 1994;34:563.
[122] Kersten H, Steffen H, Behnke JF. Surf Coatings Technol 1996;86–87:762.
[123] Eckstein W. Computer simulation of ion–solid interactions. Berlin: Springer, 1991.